NTNU

Norwegian University of
Science and Technology

Quantitative Seismic Interpretation using Rock Physics Templates - case examples from the Zumba field

Taufik Maulana

Petroleum Geosciences
Submission date: June 2016
Supervisor: Per Åge Avseth, IPT

Norwegian University of Science and Technology
Department of Petroleum Engineering and Applied Geophysics

NTNU

Norwegian University of
Science and Technology

Quantitative Seismic Interpretation using Rock Physics Templates – case examples from the Zumba field

Taufik Maulana

Petroleum Geosciences

Submission date: June 2016

Supervisor: Per Avseth, IPT

Norwegian University of Science and Technology

Department of Petroleum Engineering and Applied Geophysics

Abstract

A post drill inversion study was done by Avseth et al. (2016) after the dry well result from Zumba prospect. The AVO inversion failed in a graben setting, caused by a hard carbonate layer and associated refraction just above the target prospect. The new AVO inversion results showed a significant improvement both in AI and Vp/Vs predictions.

The objective of this thesis is to improve the understanding of the seismic response for better lithology and fluid prediction and investigate further prospectivity in the Zumba graben with the updated elastic inversion data which are calibrated to the new well.

In this study, we utilized Rock Physics Templates (RPTs) for lithology and pore fluid interpretation of well-log data and elastic inversion results. The main procedure consists of two basic steps: (1) selecting the template that is consistent with the well-log data; and (2) applying the user-defined polygon boundaries in the template to classify elastic inversion results. We also generated rock physics attribute (CPEI and PEIL) from RPT(s) that can be used to screen reservoir zone from seismic inversion.

The results show that we can potentially distinguish between different types of lithology facies in the study area. We are also able to delineate and predict potential hydrocarbon accumulations and possible remaining prospectivity in the Zumba Graben in the Norwegian Sea.

Acknowledgement

First of all, I would like to express my gratitude to the Norwegian State Educational Loan Fund and the International Master Program in NTNU for giving me a wonderful opportunity to come to Trondheim and to pursue my Master degree in this University.

I would sincerely like to thank my supervisor, Profesor Per Avseth for his expertise, support, and guidance regarding this study. I could not have asked for a better supervisor.

Additionally, I would like to thank Lara Blazevic and Amando Putra for their valuable comments and suggestions. Also big thanks for Abdul Rachim Winata for helping me on Hampson-Russel software.

Special thanks to all people that have made my stay in Norway unforgettable, International classmates, flatmates, Indonesians family in Trondheim and all of PPIT members. Two-year study abroad for me is such a priceless experience.

Finally, thanks to my beloved parents, Uni, Abang, Berto, Abut and Fia for their continuous support.

Tusen takk!

Contents

List of Figures

List of Tables

1. Introduction

Techniques for quantitative seismic data analysis have become widely used in the oil industry as these can validate hydrocarbon anomalies and give essential information during prospect evaluation and reservoir characterization. There are several techniques include offset-dependent amplitude (AVO) analysis, rock physics analysis, acoustic and elastic impedance inversion and forward seismic modeling. The objective is to first estimate elastic properties, and then use these to quantify the subsurface in terms of porosity, lithology, and fluid content.

Following Statoil's recent commercial discoveries of Yttergryta and Natalia fields, located on structural highs of the Trøndelag platform, Tullow Oil Norge AS decided to drill the high geological risk Zumba prospect, which was located in a syncline or graben setting, turned out to be a dry well. The objective of this thesis is to improve the understanding of the seismic response for better lithology and fluid prediction and investigate further prospectivity in the Zumba graben, with the updated elastic inversion data which are calibrated to the new well.

Twenty per cent of estimated resources in the Norwegian continental shelf have still to be discovered (NPD, 2011). Although the estimate for undiscovered resources has been slightly reduced from the previous resource report in 2009, the potential for finding more remains considerable (NPD, 2011). To overcome this undiscovered resources, oil industry need to look for new play models that are somewhat "outside the box" on the Norwegian continental shelf.

A post drill inversion study was done by Avseth et al. (2016) after the dry well result from Zumba prospect. The AVO inversion failed in a graben setting caused by a hard carbonate layer and associated refraction just above the target prospect. Avseth et al. (2016) study was to see if they could improve the inversion data when calibrating to the new well location. First, they did a sensitivity test to update the low-frequency model in respect to the new well 6507/11-11 log data. They subsequently reduced the angle of incidence from 50 to 40 degrees since the critical angle of the Top Lyr and Base Spekk Fm events were found to be 43 and 48 degrees, respectively. They found out that the new AVO inversion results showed a significant improvement both in AI and Vp/Vs predictions.

In this study, we utilized Rock Physics Templates (RPTs) for lithology and pore fluid interpretation of well log data and elastic inversion results. First, we did the well log data interpretation to define whether it is possible to differentiate lithology, fluids and porosity from the elastic log parameter. The next step was to validate a rock physics model to local geology using well log data, by selecting the appropriate RPT. Then we used the selected and verified RPT(s) to interpret elastic inversion results. In the end, we generated rock physics attribute (CPEI and PEIL) that can be used to screen reservoir zone from seismic inversion. The integration of these techniques allowed us to decrease the uncertainty of seismic interpretation and to investigate remaining prospectivity in the study area.

2. Geological Framework

2.1 Location

The study area which is located at the border between Halten Terrace and Trøndelag Platform in the Norwegian Sea is approximately 300 km northwest of Trondheim. It covers Grinda graben and Høgbraken horst. The area is situated within PL 591, PL 263 license, and some part is in open acreage. The targeted area and the available wells are shown in Figure 2.1.

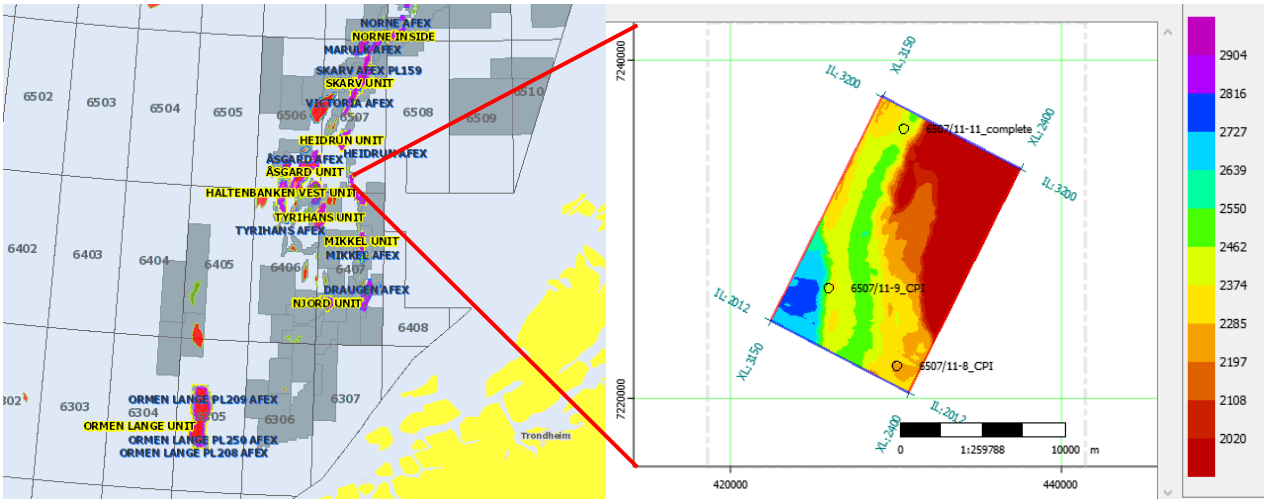

Figure 2.1: Location of the study area on the left (NPD, 2016) and well data used in this study. The color represents the horizon of the BCU.

2.2 Structural Setting

The Norwegian Sea region comprises most of the continental margin between 62^0N and $69^0$30'N. This part of the Norwegian continental shelf is described as a rifted passive continental margin (Faleide et al., 2008, Tsikalas et al., 2005). The tectonic development of the Norwegian Sea was influenced by the break-up between Norway and Greenland and plat organization of the North Atlantic in the Tertiary (NPD-bulletin 8, 1995).

The structural style of the study area was mainly formed during late Middle Jurassic-Early Cretaceous. The driving mechanism was an extension and crustal stretching that created a horst and graben structures. This area is characterized by a series of normal faults as shown in Figure 2.2. Several gas and oil discoveries are located on the Jurassic interval on the structural high of the Halten Terrace (NPD-bulletin 8, 1995).

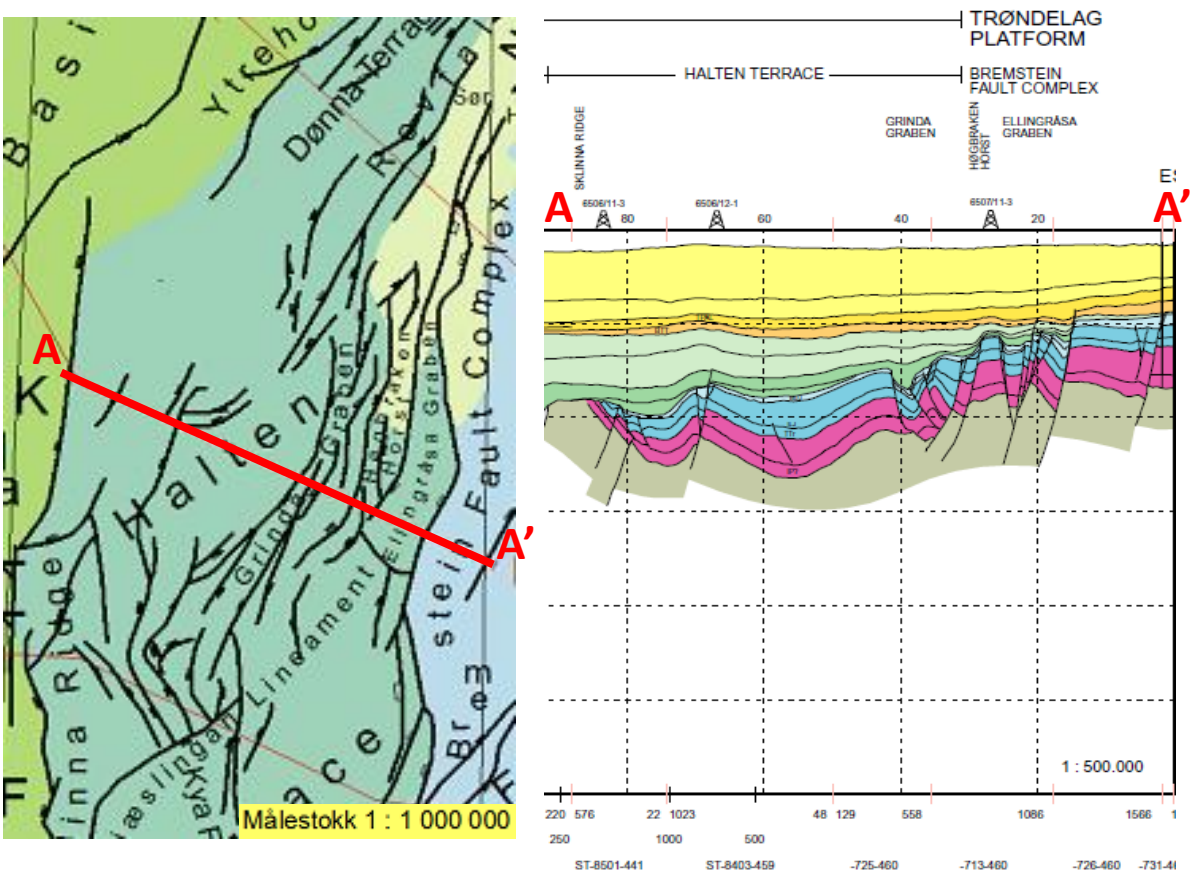

Figure 2.2: Structural elements of the study area (NPD, 1995).

2.3 Stratigraphy

The targeted interval for this study is from the Lower Jurassic to the Base Cretaceous Unconformity (BCU). The data discussed in this section is referred to nomenclature from the NPD.

2.3.1 Båt Group

The lower part of our target depth is the Båt Group which consists of Ror Fm, Tofte Fm, Tilje Fm and Åre Fm. The Båt group is interpreted to be deposited in shallow marine to deltaic environment. The Ror Fm is a dark grey mudstone and contains interbedded silty and sandy coarsening upward sequences. The Tofte Fm consists of moderately to poorly sorted coarse-grained sandstones which often shows large-scale cross bedding. The Tilje Fm is identified as a very fine to coarse-grained sandstones that are interbedded with shales and siltstones. The Åre Fm consists of alternating sandstones and claystones, in-terbedded with coals.

2.3.2 Fangst Group

The main reservoir in our study area is the Fangst group which consist of Garn Fm, Not Fm, and Ile Fm. The Ile Fm is a fine to medium and occasionally coarse-grained sandstones with varying degree of sorting. This formation is often interbedded with thinly laminated sandstones and shales. The Not Fm is generally a claystones with micronodular pyrite coarsen upwards into bioturbated fine-grained sandstones which are locally mica-rich and carbonate cemented. The Garn Fm mainly consists of medium to coarse-grained, moderately to well-sorted sandstones. The depositional environment of the Fangst group is interpreted as a shallow marine to coastal/deltaic setting. Increasing continental influence is inferred towards the Trondelag Platform to the east.

2.3.3 Viking Group

The uppermost part is the Viking Group which consists of Spekk Fm, Rogn Fm and Melke Fm. This group contains dark, grey to black, marine mudstones. Locally these argillaceous sediments are replaced by sandstones and occasionally conglomerates.

Spekk Fm has a very high organic content (mainly type II kerogen) which is a high potential to be a source rock in the study area. Rogn Fm is developed within the Spekk Fm and interpreted as shallow marine bar deposits. However, the Rogn Fm equivalent may have been deposited as gravity flows in a more deep water setting, which was the depositional model of the Zumba prospect.

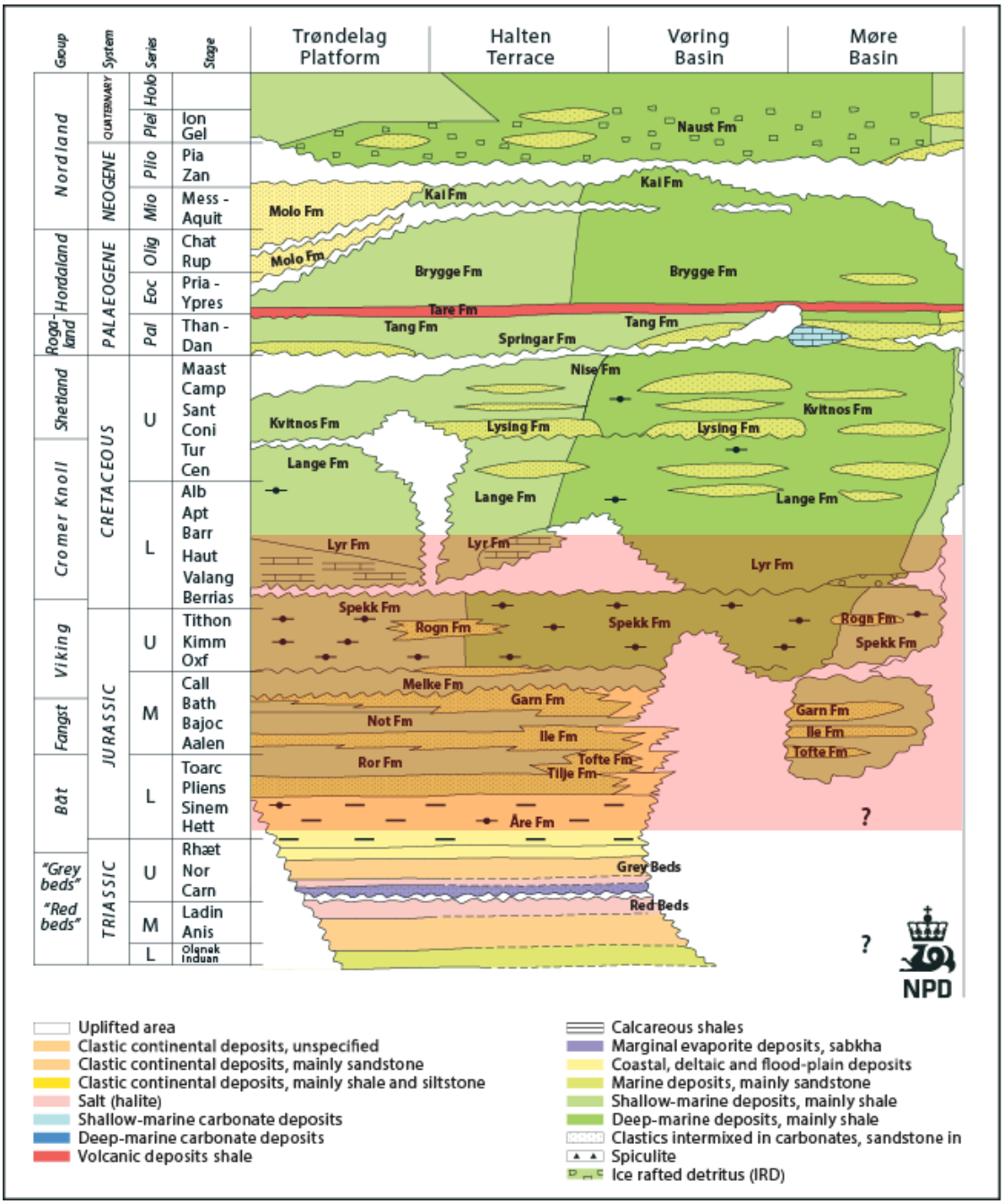

Figure 2.3: Lithostratigraphic chart of the Norwegian Sea (NPD). The focus of this study is shown in red box.

3. Background Theory

3.1 Seismic Velocities

Seismic velocities are sensitive to reservoir parameters. They are affected by porosity, pore fluid type (brine, gas or oil), lithofacies, saturation, pore pressure and other factors. P-wave and S-wave velocities which travel in homogeneous, isotropic and elastic media (Mavko et al., 2009) are given by

$$Vp = \sqrt{\frac{K+\frac{4}{3}\mu}{\rho}} \tag{1}$$

$$Vs = \sqrt{\frac{\mu}{\rho}} \tag{2}$$

Where K and μ are the bulk moduli and the shear moduli, respectively, and ρ is the density.

3.2 Fluid Substitution

This analysis is used to understand how impedance and velocity depend on pore fluids. Gassmann's relations predict how the rock modulus varies with a change of pore fluids.

The fluid effects that must be considered are the change in rock bulk density and the change in rock compressibility. The compressibility of a dry rock can be showed as the sum of the mineral compressibility and an extra compressibility due to the pore space:

$$\frac{1}{K_{dry}} = \frac{1}{K_{mineral}} + \frac{\phi}{K_{\phi}} \tag{3}$$

where ϕ is the porosity, K_{dry} is the dry rock bulk modulus, $K_{mineral}$ is the mineral bulk modulus and K_{ϕ} is the pore space stiffness.

The compressibility of saturated rock can be expressed as

$$\frac{1}{K_{sat}} = \frac{1}{K_{mineral}} + \frac{\phi}{K_{\phi} + K_{fluid} K_{mineral}/(K_{mineral} - K_{fluid})} \quad (4)$$

where K_{fluid} is the pore-fluid bulk modulus.

Equations 3 and 4 combine are proportionate to Gassmann's relations which can be expressed as

$$\frac{K_{sat}}{K_{mineral} - K_{sat}} = \frac{K_{dry}}{K_{mineral} - K_{dry}} + \frac{K_{fluid}}{\phi(K_{mineral} - K_{fluid})} \quad (5)$$

and

$$\mu_{sat} = \mu_{dry} \quad (6)$$

Hence, Gassmann's equation 5 and 6 predict the bulk modulus will change if the fluid changes, but the shear modulus will not for an isotropic rock.

3.3 Rock physics models for dry rock

3.3.1 Elastic bounds

Generally rock physics models need to define three types of information:

1) The volume fractions of the various constituents
2) The elastic moduli of the various phases
3) The geometric details of how the phases are arranged relative to each other

The geometric details of the rocks have never been adequately incorporated into the theoretical model. Any attempt to do so, usually leads to approximations and simplifications. When we only specify the volume fractions and their elastic moduli, without geometric details, then we can only predict the upper and lower bounds on the moduli. At any given volume fraction of constituents, the effective modulus of the mixture will fall between the bounds as we can see in Figure 3.1 (Avseth et al., 2005).

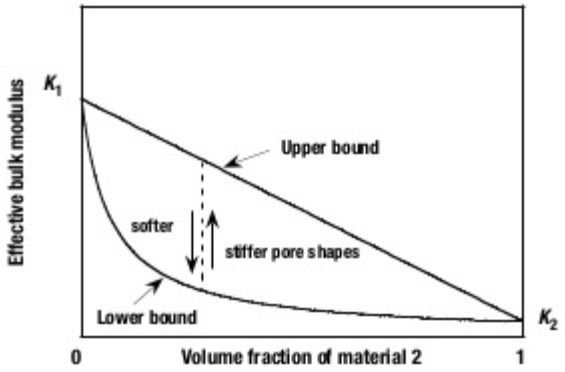

Figure 3.1: Conceptual illustration of bounds for the effective elastic bulk modulus of a mixture of two minerals (Avseth et al.,2005).

3.3.2 The Voigt and Reuss bounds

The simplest, but not necessarily the best bounds are the Voigt (1910) and Reuss (1929) bounds. The *Voigt upper bound* on the effective elastic modulus, Mv, of a mixture of *N* material phases (Avseth et al., 2005) is

$$M_v = \sum_{i=1}^{N} f_i M_i \tag{7}$$

where f_i is the volume fraction of the *i*th constituent and M_i is the elastic modulus of the *i*th constituent. This bound gives the ratio of average stress to average strain when all constituents are assumed to have the same strain. Thus, it is called the *isostrain* average. There is no mixture of a constituent that is elastically *stiffer* than the Voigt bound.

The *Reuss lower bound* of the effective elastic modulus, M_R , is

$$\frac{1}{M_R} = \sum_{i=1}^{N} \frac{f_i}{M_i} \tag{8}$$

The Reuss bound gives the ratio of average stress to average strain when all constituents are assumed to have the same stress. It is called the *isostress* average. There is no mixture of a constituent that is elastically *softer* than the Reuss bound. The Reuss average can be used to describe the effective moduli of a suspension of solid grains in a fluid.

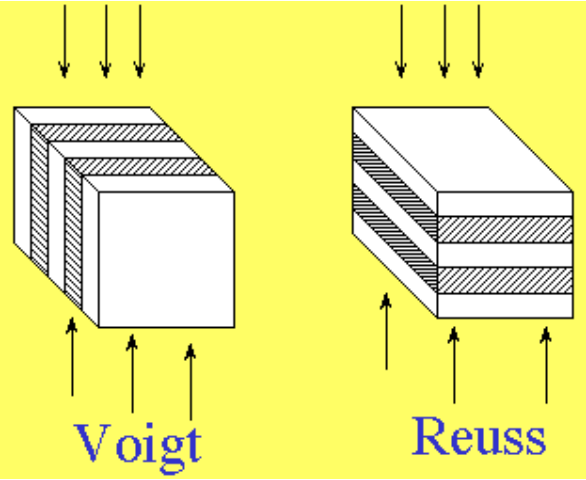

Figure 3.2: Geometric of the two phase in Voigt and Reuss bounds (Wisconsin, 2004).

3.3.3 Hashin-Shtrikman bounds

The *Hashin-Shtrikman bounds* give the narrowest possible range of elastic moduli without specifying the geometries of the constituents. It is the best bounds for an isotropic elastic mixture (Avseth et al., 2005). The Hashin-Shtrikman bounds for a mixture of two constituents are given by

$$K^{HS\pm} = K_1 + \frac{f_2}{(K_2 - K_1)^{-1} + f_1(K_1 + \frac{4\mu_1}{3})^{-1}} \tag{9}$$

$$\mu^{HS\pm} = \mu_1 + \frac{f_2}{(\mu_2 - \mu_1)^{-1} + 2f_1(K_1 + 2\mu_1)/[5\mu_1\left(K_1 + \frac{4\mu_1}{3}\right)]} \tag{10}$$

where $K_1$and K_2 are the bulk moduli of individual phase, $\mu_1$and $\mu_2$are the shear moduli of individual phases, f_1 and f_2 are the volume fractions of individual phases.

Upper and lower bounds are computed by interchanging which material is subscripted 1 and which is subscripted 2 (Avseth et al., 2005). The lower bound is when the *softest* material is subscripted 1 and the upper bound is when the *stiffest* material is subscripted 1. The physical interpretation of the Hashin-Shtrikman bounds for bulk modulus of a two phase material is shown in Figure 3.3.

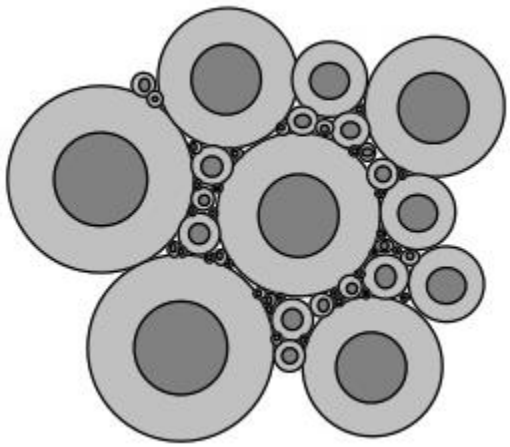

Figure 3.3: Physical interpretation of the Hashin-Shtrikman bounds (Avseth et al., 2005).

3.3.4 Hertz-Mindlin theory

This theory defines that the elastic moduli are modeled as an elastic sphere pack subject to confining pressure. The elastic moduli are seen to depend on the contact properties between the grains.

$$K_{HM} = \left[\frac{n^2(1-\phi_c)^2\mu^2}{18\pi^2(1-v)^2}P\right]^{1/3} \quad (11)$$

$$\mu_{HM} = \frac{5-4v}{5(2-v)}\left[\frac{3n^2(1-\phi_c)^2\mu^2}{2\mu^2(1-v)^2}P\right]^{1/3} \quad (12)$$

where K_{HM} and μ_{HM} are the dry rock bulk and shear moduli, respectively, at critical porosity ϕ_c(i.e.,depositional porosity); P is the effective pressure (i.e.,the difference between the overburden pressure and the pore pressure); μ and v are the shear modulus and Poisson's ratio of the solid phase; and n is the coordination number (the average number of contacts per grain).

The Poisson's ratio can be expressed in terms of the bulk (K) and shear (μ) moduli as follows:

$$v = \frac{3K-2\mu}{2(3K+\mu)} \quad (13)$$

Effective pressure versus depth is obtained with the following formula:

$$P = g\int_0^Z(\rho_{b-}\rho_{fl})dz \quad (14)$$

where g is the gravity constant, and ρ_b and $\rho_{fl}$are the bulk density and the fluid density, respectively, at a given depth, Z (Avseth et al., 2005) .

The coordination number,*n*, depends on porosity, as shown by Murphy (1982). The relationship between coordination number and porosity can be approximated by the following empirical equation :

$$n = 30 - 34\phi + 14\phi^2 \quad (15)$$

3.4 AVO

Amplitude Versus offset (AVO) was first introduced by Ostrander in 1984. He showed that gas sands would cause an amplitude variation with offset. He also found that this change was associated with the decreased Poisson's ratio caused by the presence of the gas. A year later, Shuey (1985) confirmed mathematically that Poisson's ratio was the elastic constant related to the offset-dependent reflectivity for incident angles up to 30^o via approximations of the Zoeppritz equations.

Today, the AVO analysis has become very popular in the oil industry, as widely used in hydrocarbon detection, lithology identification, and fluid parameter analysis. AVO analysis attempts to use the offset-dependent variation of P-wave reflection coefficients to detect and/or estimate anomalous contrasts in shear-wave velocities and densities across an interface.

AVO is more challenging than conventional seismic because AVO is conducted on noisier prestack data and depends on the basic petrophysical data signal that is obscured by wave propagation. The factors that affect seismic amplitudes must be understood and considered and then data must be processed in such a way that the changes in amplitude can be reliably interpreted as changes in rock and fluid properties. Table 3.1 lists the factors that affecting seismic amplitudes.

The success of any AVO analysis depends on understanding the various distortion effects that contaminate offset- dependent reflectivities and on removing those effects effectively. It is important to note that as long as AVO is used in practice as a qualitative anomaly-hunting tool, only relative amplitudes as a function of offset need be preserved. However, if the objective is to invert AVO information for absolute rock properties, such as impedances and velocities, true amplitudes and phase (or additional a priori information) are required (Chopra and Castagna et al., 2014).

Table 3.1: Factor affecting seismic amplitude (Chopra and Castagna, 2014).

Physical effects (wave propagation/geologic effects)	Acquisition-related effects (source-generated)	Noise (related to faulty equipment or bad acquisition procedures)	Processing-induced artifacts
†Spherical spreading	Source strength, radiation pattern, and consistency	Coherent, ambient noise	Residual NMO/NMO stretch
†Transmission	†Receiver coupling	Unbalanced noise	Statics
†Attenuation, dispersion	†Receiver array (directivity)	Drilling noise	Radon-transform applications
†Mode conversion	Instrumentation	High-frequency noise (faulty electronics)	*f-k* filtering
†Temporal tuning	Sampling (time and offset)	Low-frequency noise (cable problem)	Noise reduction
†Multiples (interbed and surface)	Offset range	Sidescatter	†DMO
†Reflector curvature			Migration
†Anisotropy			AGC
			Deconvolution

3.4.1 The Reflection Coefficient

Consider two semi-infinite isotropic homogeneous elastic media in contact at a plane interface. Then, an incident compressional plane wave impinges on this interface. A reflection at an interface disperses energy partition from an incident P-wave to a reflected P-wave, a transmitted P-wave, a reflected S-wave, and a transmitted S-wave as shown in Figure 3.4. The angles of incident, reflected, and transmitted rays at the boundary are related to Snell's law as:

$$p = \frac{sin\theta 1}{Vp1} = \frac{sin\theta 2}{Vp2} = \frac{sin\phi 1}{Vs1} = \frac{sin\phi 2}{Vs2} \quad (16)$$

where $Vp1$ and $Vp2$ are P-wave velocities, and $Vs1$ and $Vs2$ are S-wave velocities in medium 1 and 2, respectively. $\theta 1$ is the incident P-wave angle, $\theta 2$ is the transmitted P-wave angle, $\phi 1$ is the reflected S-wave angle, $\phi 2$ is the transmitted S-wave angle and p is the ray parameter.

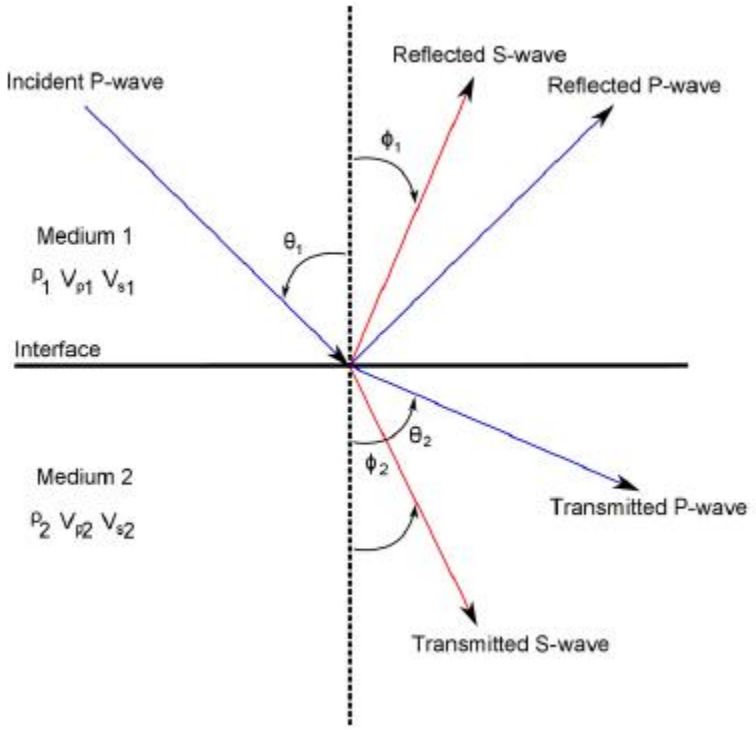

Figure 3.4: Reflections and transmissions at a single interface.

The reflection coefficient is a numerical measure of the amplitude and polarity of the wave reflected from an interface, relative to the incident wave. For a wave that hits a boundary at normal incidence, the expression of the reflection coefficient is:

$$Ro = \frac{Z2-Z1}{Z2+Z1} \quad (17)$$

where:

Z = the continuous P-wave impedance profile

Z1 = impedance of medium 1 = ρ1 . $Vp1$

Z2 = impedance of medium 2 = ρ2 . $Vp2$

ρ1 = density of medium 1

ρ2 = density of medium 2

3.4.2 Approximations of the Zoeppritz equations

Zoeppritz equations describe the reflection coefficient as a function of reflection angle at the single interface for plane elastic waves. Several attempts have been made to develop approximations to the Zoeppritz equations. A well-known approximation is given by Aki and Richards (1980), assuming weak layer contrasts:

$$R(\theta_1) \approx \frac{1}{2}(1 - 4p^2Vs^2)\frac{\Delta\rho}{\rho} + \frac{1}{2cos^2\theta}\frac{\Delta V_p}{V_p} - 4p^2{V_s}^2\frac{\Delta V_s}{V_s} \qquad (18)$$

where

$$p = \frac{sin\theta_1}{V_{p1}}$$

$$\theta = (\theta_1 + \theta_2)/2 \approx \theta_1$$

$$\Delta\rho = \rho_2 - \rho_1$$

$$\rho = (\rho_2 + \rho_1)/2$$

$$\Delta V_p = V_{p2} - V_{p1}$$

$$\Delta V_p = (V_{p2} + V_{p1})/2$$

$$\Delta V_s = V_{s2} - C$$

$$\Delta V_s = (V_{s2} + V_{s1})/2$$

In the equations above, p is the ray parameter, $\theta_1$is the angle of incidence, and $\theta_2$is the transmission angle; $V_{p1}$and V_{p2} are the P-wave velocities above and below a given interface, respectively. V_{s1} and $V_{s2}$are the S-wave velocities, while $\rho_1$and $\rho_2$are densities above and below this interface.

Shuey did further approximation which assumes Poisson's ratio to be the elastic property most directly related to the angular dependence of the reflection coefficient (Shuey, 1985) as given by:

$$R(\theta) \approx R(0) + Gsin^2\theta + F(tan^2\theta - sin^2\theta) \tag{19}$$

where

$$R(0) = \frac{1}{2}\left(\frac{\Delta V_p}{V_p} + \frac{\Delta\rho}{\rho}\right)$$

$$G = \frac{1}{2}\frac{\Delta V_p}{V_p} - 2\frac{{V_s}^2}{{V_p}^2}\left(\frac{\Delta\rho}{\rho} + 2\frac{\Delta V_s}{V_s}\right)$$

$$= R(0) - \frac{\Delta\rho}{\rho}\left(\frac{1}{2} + 2\frac{{V_s}^2}{{V_p}^2}\right) - \frac{4{V_s}^2}{{V_p}^2}\frac{\Delta V_s}{V_s}$$

and

$$F = \frac{1}{2}\frac{\Delta V_p}{V_p}$$

where $R(0)$ is the normal incident reflection coefficient, $G$is the AVO gradient which describes the variation at intermediate offsets and F dominates the far offsets, near critical angle.

The approximation becomes simplified into two terms because the range of angles available for AVO analysis is usually less than 40^o:

$$R(\theta) \approx R(0) + Gsin^2\theta \tag{20}$$

3.4.3 AVO cross-plot analysis

AVO cross-plot analysis is a technique that uses cross-plots of intercept (R(0)) versus gradient (G) from Shuey's approximation to interpret AVO attributes. This analysis can give a better understanding of the rock properties than by analyzing the standard AVO curves.

The first AVO classification technique was introduced by Rutherford and Williams (1989). They suggested a classification of AVO responses for a different type of gas sandstones and made it into three AVO classes. It was based on where the top of the gas sands will be located in a R(0) versus G cross-plot.

The cross-plot is divided into four quadrants as we can see in Figure 3.5. The 1st quadrant is where R(0) and G are both positive values (upper right quadrant). The 2nd quadrant is where R(0) is negative and G is positive (upper left quadrant). The 3rd quadrant is where R(0) and G are both negative values (lower left quadrant). Finally, the 4th quadrant is where R(0) is positive and G is negative (lower right quadrant). The quadrant numbers must not be confused with the AVO classes (Avseth et al., 2005)

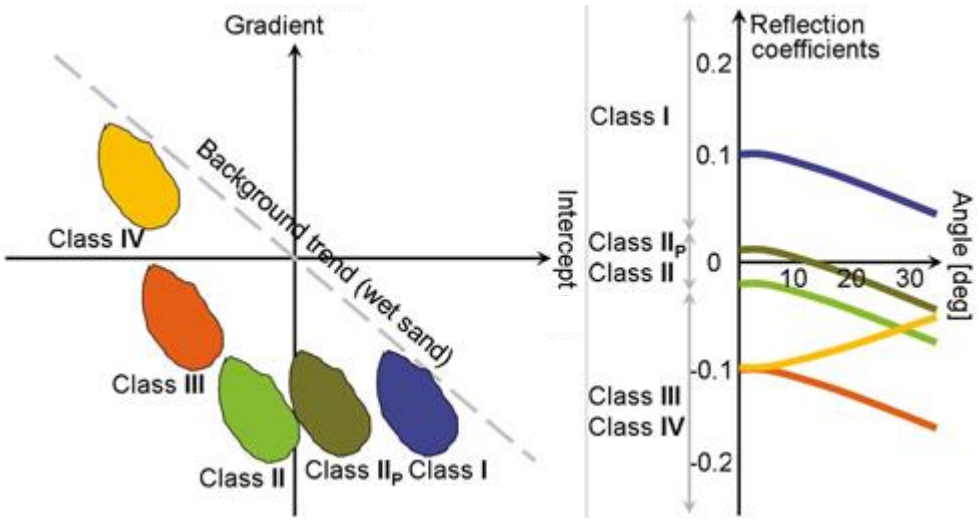

Figure 3.5: Crossplot of the intercept versus gradient (CGG).

Class I (blue colour) plots in the 4th quadrant which represent hard events with relatively high impedance and low Vp/Vs ratio compared with the cap-rock. Class II is typical sands with a weak intercept that usually produce dim spots on stacked sections. Class III is associated with soft sands saturated with hydrocarbons. It is the AVO category which is commonly correlated with bright spots. Class IIp established by Ross and Kinman in 1995 which is a sub-class of class II. It has positive intercept and a negative gradient which generate a polarity change. This class will disappear on full stack sections.

Castagna and Swan (1997) added the classification of Rutherford and Williams with a 4th class. This Class plots in the 2nd quadrant. Class IV represents soft gas sands capped by relatively stiff shales characterized by Vp/Vs ratios slightly higher than in the sands. This class is quite rare for gas sands (Avseth et al., 2005). Table 3.2 summarizes all of the AVO classes with their characteristic.

Table 3.2: AVO classes, after Rutherford and Williams (1989), extended by Castagna and Smith (1994), and Ross and Kinman (1995).

Class	Relative Impedance	Quadrant	R(0)	G	AVO product
I	High-impedance sand	4th	+	-	Negative
IIp	No or low contrast	4th	+	-	Negative
II	No or low contrast	3rd	-	-	Positive
III	Low Impedance	3rd	-	-	Positive
IV	Low Impedance	2nd	-	+	Negative

3.5 Seismic Inversion

Ambiguities in lithologic and fluid identification based only on normal incidence impedance (ρV) can be often be effectively removed by adding information about Vp/Vs related attributes, e.g. from non-normal incidence (Ostrander, 1984; Smith and Gidlow, 1987).

Seismic Impedance inversion is one of many approaches to lithofacies identification. Mukerji et al. (1998) defined a far offset impedance which includes

information about the Vp/Vs ratio and removes classification ambiguities inherent in zero offset impedance.

$$Ie(\theta) = Vp^{1+tan^2\theta}\rho^{1-4(\frac{Vs}{Vp})^2sin^2\theta}Vs^{-8(\frac{Vs}{Vp})^2sin^2\theta} \quad (21)$$

One problem of the original elastic impedance is that its dimension varies with incident angle. Whitcombe et al. (2002) introduced the Extended Elastic Impedance (EEI) approach which is a normalization of the elastic impedance to acoustic impedance so the dimensions would be the same as the acoustic impedance for any angle. They also introduced the chi angle instead of the angle of incident, where the chi angle is a rotation in the intercept vs. gradient cross-plot domain. From equation (22) we can see that the EEI equivalent to x=0° is acoustic impedance.

$$EEI(x) = V_{po}\rho_o[\,(\frac{V_p}{V_{po}})^{(\cos x+sinx)}(\frac{\rho}{\rho_o})^{(cosx-4Ksinx)}(\frac{V_s}{V_{so}})^{-8Ksinx}] \quad (22)$$

3.6 Rock physics templates

Rock physics draws a relationship between geology and seismic data. It helps to explain reflection signatures by quantifying the elastic properties of rocks and fluids. By creating models, it can assist us to understand the behaviour of the reservoir and non-reservoir zones. RPT's were introduced by Ødegaard and Avseth (2004) and widely used to screen or classify seismic inversion data for hydrocarbon prospects during exploration.

Figure 3.6 shows the RPT concept. The template encompasses models of different lithologies and fluid scenarios that are expected in the area of interest. These

models can be used as a toolbox for efficient lithology and pore fluid interpretation of well log data and elastic inversion results. The template includes porosity trends for different lithologies, and increasing fluid saturation for sands. The arrows indicate different geologic trends.

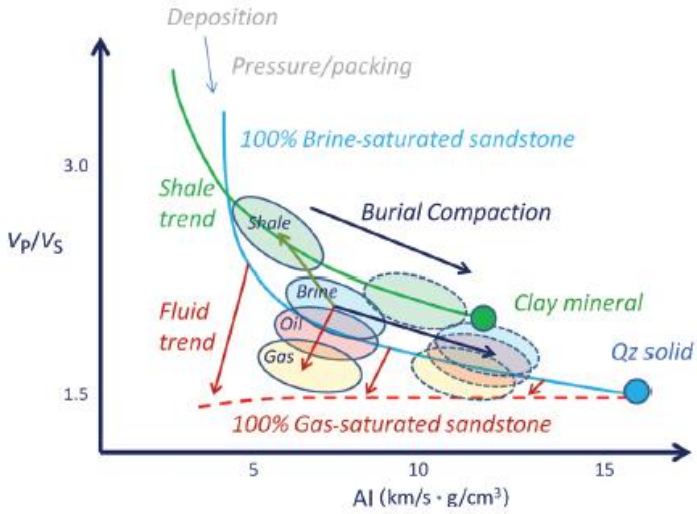

Figure 3.6: RPT anatomy model concept for brine and gas saturated sandstones, and for shales (Avseth and Veggeland, 2015).

Water-saturated sands at the deposition will have very high Vp/Vs because of the very low shear modulus. However, the Vp/Vs ratio will decrease rapidly with increasing pressure, depth and burial. In the other hand, AI will increase as grains are packed together and cemented. The effect of mineralogy will be significant in RPT because clays and carbonates have higher Vp/Vs than quartz. However increasing shaliness will have different effect on AI depending on if the clay particles are laminating or pore filling. AI will increase if the clay particles are pore filling, and it will decrease if the clay particles are laminating. Finally, AI and Vp/Vs will decrease with increasing hydrocarbon saturation.

3.7 Defining rock physics attribute

Avseth et al. (2014) introduced the CPEI attribute defined as the distance away from a brine-saturated sandstone model in an RPT domain. The sandstone model was made from Dvorkin-Nur contact cement theory combined with upper-bound Hashin-Shtrikman, also referred to as *increasing cement model* (Avseth et al., 2005).

A mathematical function is fitted to sandstone model in the Vp/Vs versus AI domain:

$$y = f(x) \tag{23}$$

where y=Vp/Vs , x=AI , and f(x) is Vp/Vs expressed as a function of AI. Then we define attribute as a function that quantifies the deviation away from this line

$$w = xo + k.[f(x) - y] \tag{24}$$

where xo act as a scale so the data will not have a zero value but equal to a reference value and k will tune the deviation away.

A good match of water saturated sandstone model can be obtained by polynomial fit in the natural logarithmic domain of AI versus Vp/Vs:

$$f(x) = \exp(a.ln^4x + b.ln^3x + c.ln^2x + d.lnx + e) \tag{25}$$

Based on the comparison between brine-filled sandstone model and fitting function, where the fitting parameters are as follows (Avseth et al., 2015):

$$a = 0.805, b = -7.276, c = 24.581, d = -36.993, e = 21.519 \quad (26)$$

Furthermore, we define xo = 6.9 km/s.g/cm3 as the reference impedance value and k = -3.5 then by inserting the fitting function from equation 26 into equation final CPEI attribute can be expressed as :

$$CPEI = 6.9 - 3.5(\exp[a.ln^4AI + b.ln^3AI + c.ln^2AI + d.lnAI + e) - \frac{Vp}{Vs}] \quad (27)$$

CPEI attribute is sensitive to fluid saturation. Therefore, it will highlight fluid related anomalies, and correlates with fluid softening due to the presence of hydrocarbons. Hydrocarbon anomalies will have lower values than 6.9 while brine sand, shales, and carbonates will have values of 6.9 or higher (Avseth et al., 2015).

The other attribute will represents the deviation from a straight line running parallel with constant shear moduli in the Vp/Vs versus AI. So we use straight line function as an input into equation

$$f(x) = a.x + b \quad (28)$$

to obtain PEIL attribute which is expressed as :

$$PEIL = 6.9 + 3.5\ (\ a.AI + b - \frac{Vp}{Vs}) \quad (29)$$

This attribute correlates with rock stiffness and is not dependent on pore fluid content. It also will be more or less orthogonal to the fluid trend.

4. Methodology

The general workflow used for the thesis is divided into six major stages which can be seen in Figure 4.1.

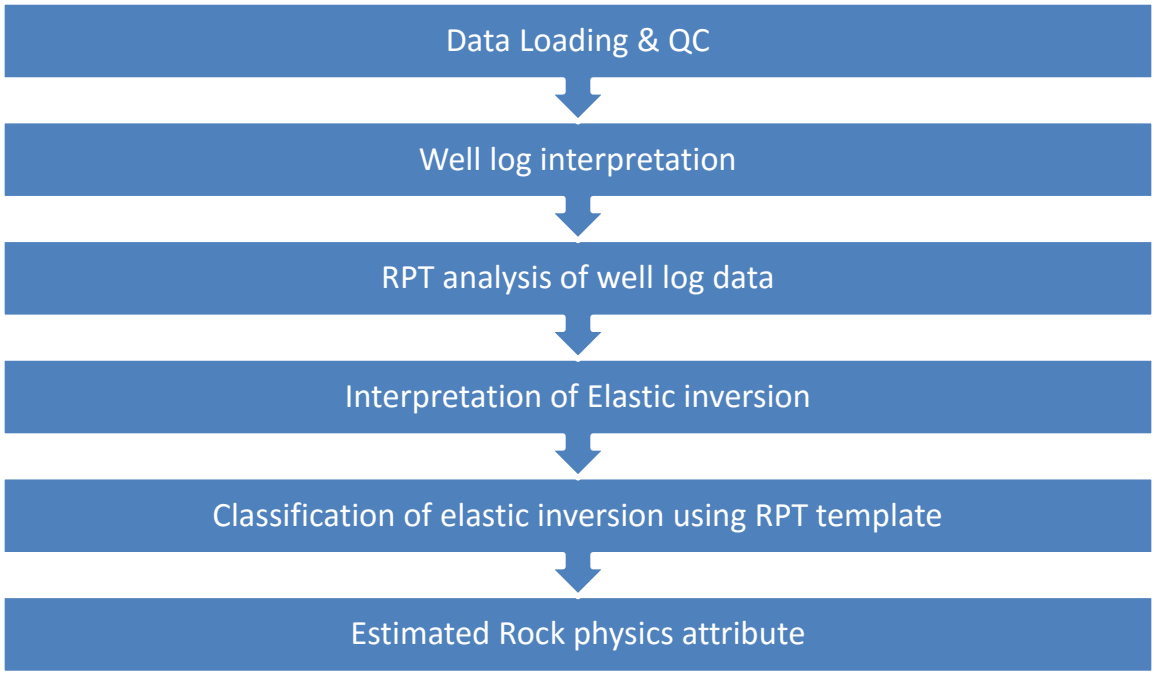

Figure 4.4: The main project workflow

4.1 Data

The seismic data used for the thesis is a broadband data of simultaneous AVO inversion which inverts partial stack directly for AI, Vp/Vs, and density, using a 3-term Aki Richard approximation to the Zoeppritz equation (Ma 2002; Rasmussen et al. 2004). The seismic cube covers around 101 km^2.

There are 3 wells available for this study. Two discovery wells and one dry well. The discoveries wells are 6507/11-8 and 6507/11-9. Well 6507/11-8 is located in the eastern part of the Halten Terrace, just north of the Midgard discovery. It was drilled on the Yttergryta structure with the primary objective to identify gas in Garn and Ile Formations. The secondary objective of well 6507/11-8 was to

acquire data and test for possible hydrocarbons in the Tilje and Åre Formations (NPD).

Well 6507/11-9 was drilled on the Natalia prospect in the Grinda Graben, ca. 5 km north of the Midgard Field in the Norwegian Sea. It was drilled up-dip from the previously drilled 6507/11-4 on the same structure. The primary objective of the well was to prove the presence of hydrocarbons in the Jurassic sandstones in the Fangst Group. The secondary target was to examine the hydrocarbon migration route in the prospect area (NPD)

The third well is 6507/11-11 which was drilled last year in 2015 on the Zumba prospect in the Grinda Graben just north of the Yttergryta discovery. It was targeting hydrocarbons in the Rogn Fm sands of the Upper Jurassic age. The play model was a stratigraphic trap confined by a graben. The result was dry as there was no hydrocarbon content penetrated by the well and only 4 - 5 m thin Rogn Fm sandstone embedded in the Spekk Fm shales.

4.2 Software

Two main softwares were used in this study for data calculation, analysis, and display.

Matlab is a numerical computing environment and programming language software which can be used to display numerical data from any source.

Hampson-Russell is a geophysical software which encompasses all aspects of seismic exploration and reservoir characterization including AVO and RPT analysis.

4.3 Data Loading & QC

Reading seismic data header before loading the data is a crucial step. It is important to recognize the parameter of the seismic in order to get the correct data. The seismic data set for this thesis are listed in table 4.1.

Table 4.1: Available seismic data.

Type	Format
AI inversion	SEGY
Vp/Vs inversion	SEGY
Density inversion	SEGY

All of the seismic 3D data have the same geometric parameters as can be seen in Figure 4.2.

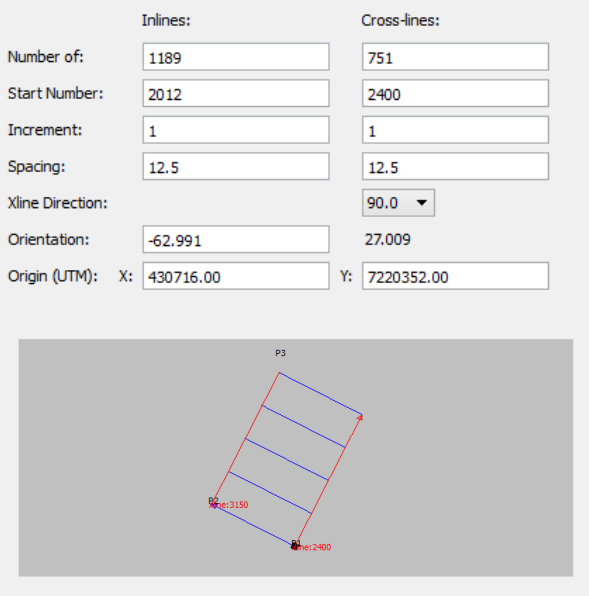

Figure 4.2: Seismic geometry parameter.

The current status of the three wells and the well log data availability is listed in table 4.2.

Table 1.2: Well log data availability.

Official name	Short name	Well content	Well log curve provided
6507/11-8 (Yttergryta)	Well 8	Gas Well	GR,DTC,DTS,RHOB,NPHI,SW,RDEP
6507/11-9 (Natalia)	Well 9	Gas Well	GR,DTC,DTS,RHOB,NPHI,SW,RDEP
6507/11-11 (Zumba)	Well 11	Dry	GR,DTC,DTS,RHOB,NPHI,RDEP

Compressional slowness (DTC), shear slowness (DTS) and density (RHOB) log curves were used to give information about lithology and fluids and to create elastic parameter such as Vp/Vs. These log curves cover the targeted zone for this study.

4.4 Well log Interpretation

Petrophysical evaluation and rock physics analysis were done in this stage. The evaluation was undertaken for the three wells available in this study. Each well has good quality of P-wave, S-wave velocity and density log which were used to retrieve elastic parameter and other rock physics attributes. Acoustic impedance (AI) and Vp/Vs are some of the outputs of those log combination that is useful for predicting lithology and fluid contents.

Gamma Ray, resistivity, and RHOB-NPHI log are also contributing to finding hydrocarbon bearing zones in this area. In well 6507/11-9, the gas saturated zone occurs at 2608 – 2638 m (MD from KB) in the Garn Fm. Two gas saturated zone also showed in well 6507/11-8 at 2424 – 2447 m (MD from KB) and 2460 – 2509 m (MD from KB). On the other hand, well 6507/11-11 showed no indication of hydrocarbon bearing zone. Figure 4.3, Figure 4.4, and Figure 4.5 show the available logs and the interpreted gas saturated zone on well 6507/11-9, 6570/11-8 and 6507/11-11, respectively. Other logs such as Vcl, saturation, RMED, and RMIC are also available in each well.

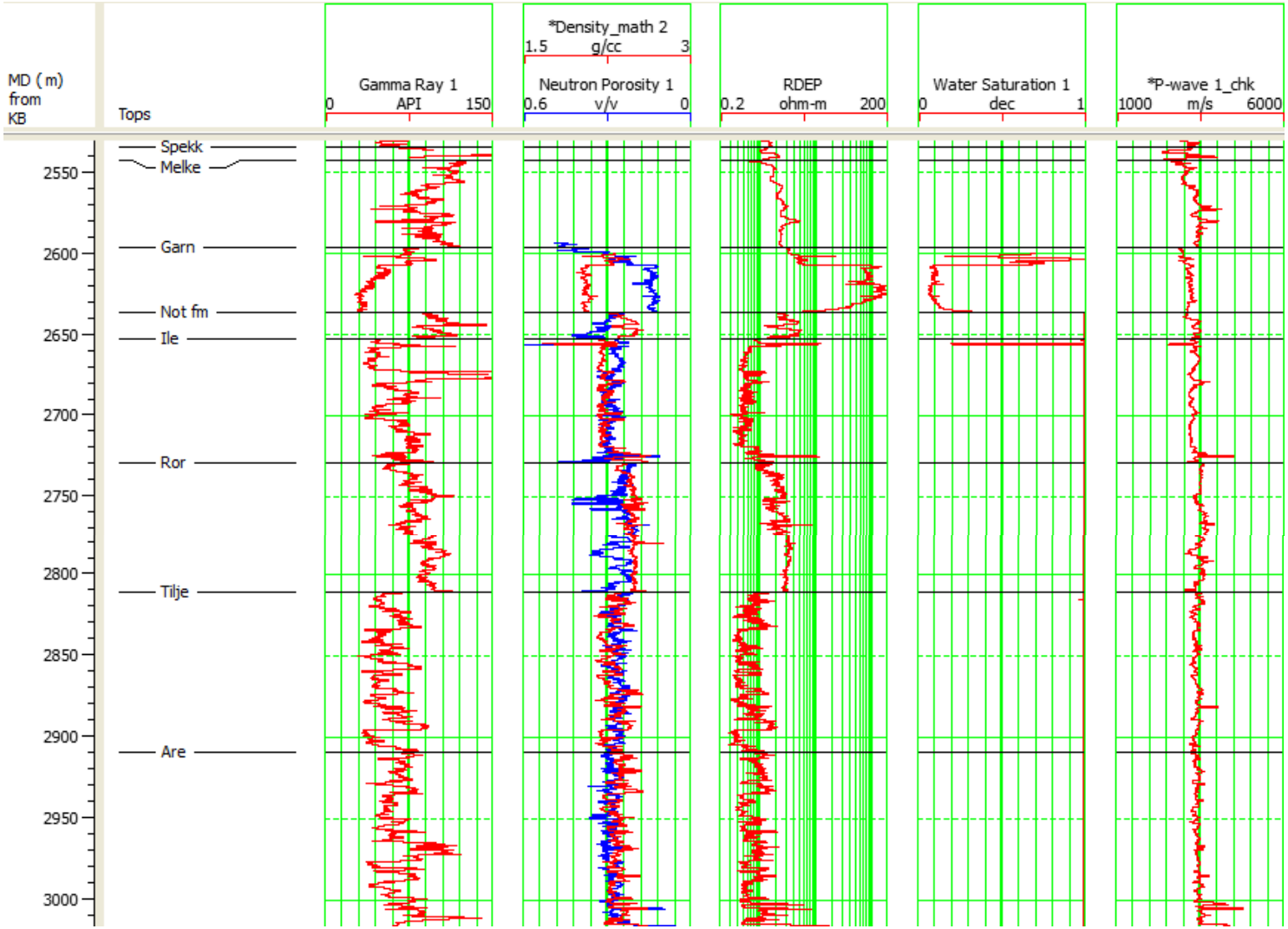

Figure 4.3: Available logs for well 6507/11-9 (from left GR, density-neutron, resistivity, water saturation, P-wave velocity).

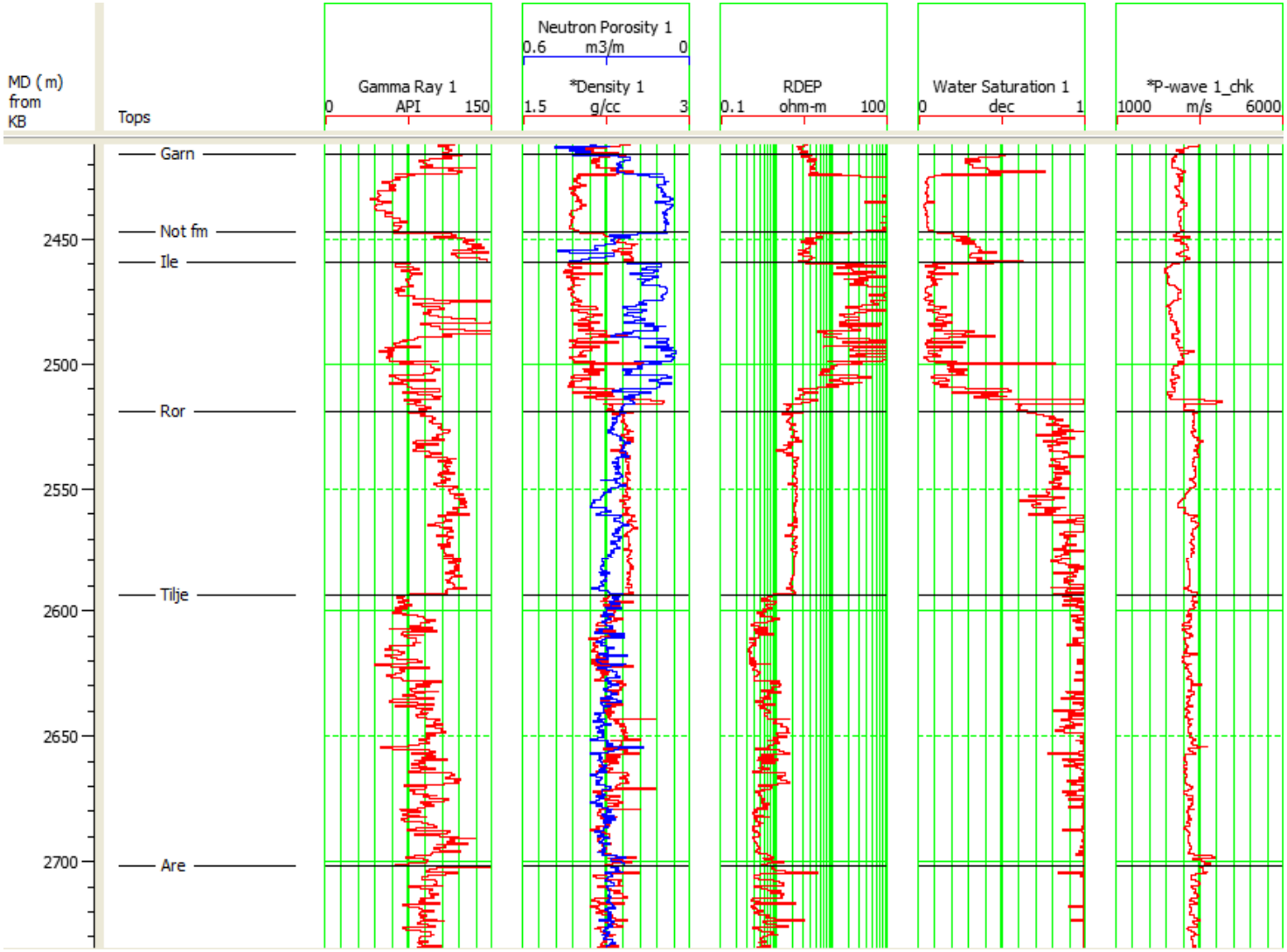

Figure 4.4: Available logs for well 6507/11-8 (from left GR, density-neutron, resistivity, water saturation, P-wave velocity).

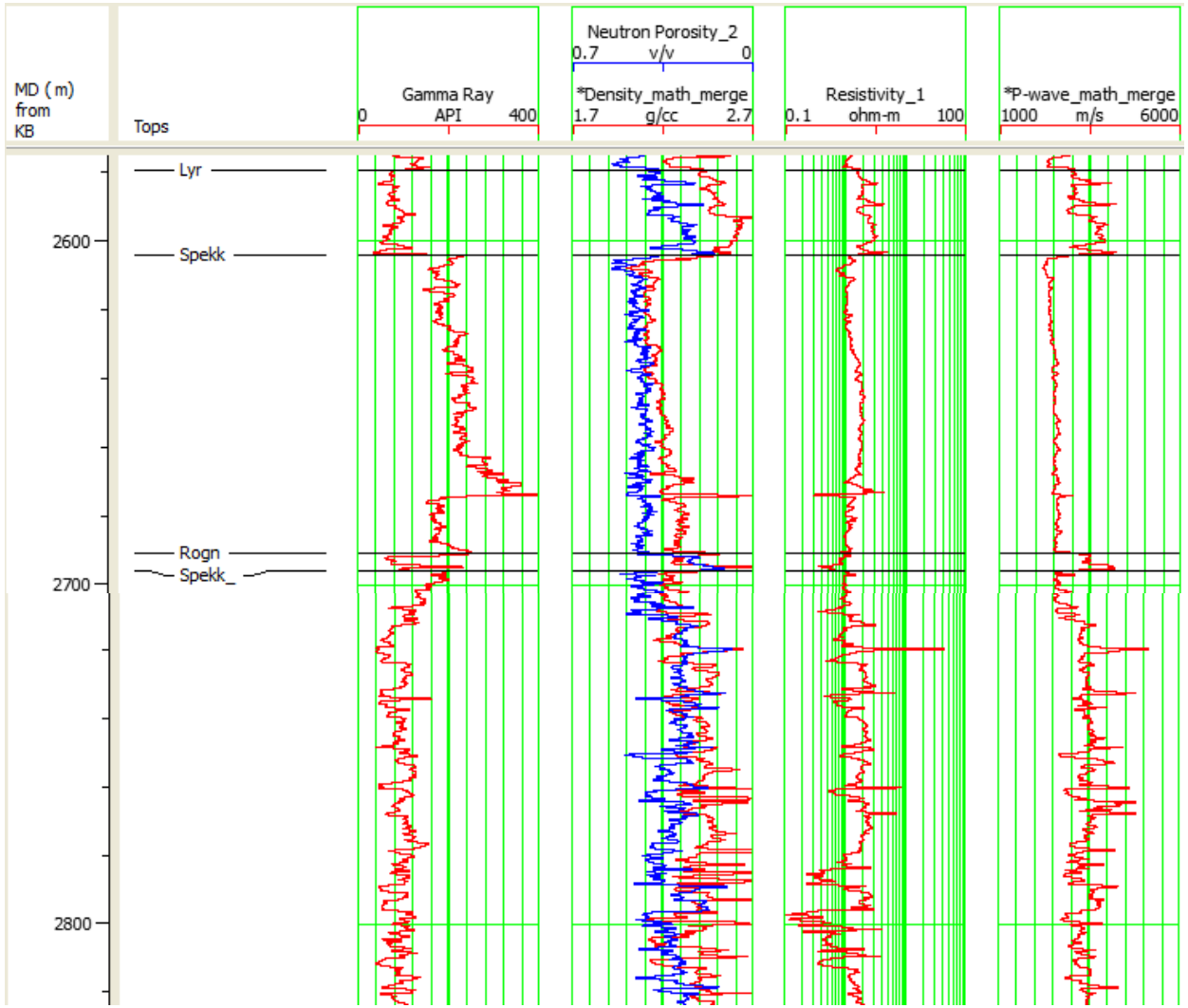

Figure 4.5: Available logs for well 6507/11-11 (from left GR, density-neutron, resistivity, P-wave velocity).

4.4.1 Gamma ray log

Gamma ray log measure natural radiation emitted by the rock formations. This log is used to identify lithology and depositional facies via log shapes. In addition, gamma ray can be considered as a good shale indicator. Clean sandstones normally have low radioactive mineral hence represent low gamma ray reading. High gamma sandstones occur due to high mica, feldspar or heavy radioactive minerals such zircon and apatite.

From Figure 4.3 and Figure 4.4 we can observe the transition between Garn Fm and Not Fm around 2640 m for well 6507/11-9 and 2445 m for well 6507/11-8. This gamma ray deflection interpreted as a barrier between sandstones (lower API) and shale formation (higher API).

Low gamma ray value (30-50 API) normally indicate as clean sand formation as we can see from well 6507/11-9 for depth interval 2600 m - 2637 m and well 6507/11-8 for depth interval 2415 m - 2446 m. The gamma ray value goes slightly higher if the sand formation contains more shale as we can see in Ile formation from well 6507/11-9. Well 6507/11-11 only encountered a thin sandstone unit of 4-5 meters near the base of the Spekk Fm, as can been in the gamma ray log. Below Spekk Fm the gamma ray value is evenly higher than 60 API.

4.4.2 Density & Neutron Log

Density log measures the electron density of a formation. This log mainly used to determine the porosity and good lithology indicator in certain formations (eg. Anhydrite,coal,halite). It also can be used to identify hydrocarbon type and trends. Densities will normally lie between 1.90 and 3.10 g/cc (except for coal, 1.40 g/cc).

Neutron log mainly measures hydrogen concentration in a formation. It is used to determine porosity and lithology in combination with other logs. Neutron log also can be used to identify certain mineralogies and gas bearing formations. Lower neutron value normally indicated as porous formation.

The combination between density and neutron log is the most common combination of logs for porosity, lithology and gas identification. The crossover between these logs (density porosity is greater than neutron porosity) is mainly used to detect a gas bearing formation.

From Figure 4.3 and Figure 4.4 we can observe the crossover from well 6507/11-9 for depth interval 2608 m – 2637 m and well 6507/11-8 for depth interval 2424 m – 2447 m and 2460 m – 2510 m. There is no crossover value between density and neutron from well 6507/11-11 as we can see in Figure 4.5.

4.4.3 Resistivity log

Resistivity log measures the subsurface electrical resistivity, which is the ability to impede the flow of electric current. The primary applications for the resistivity logs are fluid saturations and hydrocarbon thickness (net pay). The common assumptions are that the rock matrix (non-shaly), oil and gas do not conduct electricity whereas water in the pore space will conduct electricity. Hence, resistivity value will be high if there is an indication of hydrocarbon bearing rock.

We can see from Figure 4.3 and Figure 4.4 that the Garn Fm has a high value of resistivity (>100-ohm m). This is typically an indication of hydrocarbons, because in hydrocarbons bearing formations, higher porosities tend to hold less irreducible water and therefore read higher resistivity. On the other hand, there is no indication of a high value of resistivity from well 6507/11-11.

4.4.4 P-wave velocity

P-wave log measures the travel time of an elastic wave through the formation to yield the velocity (v) or the slowness (Δt) of the formation. The primary applications of the P-wave log are porosity determination and rock mechanics. In addition, it is often used to identify gas bearing rocks because P-wave normally will decrease significantly in gas. It is found that compressional wave is sensitive to the saturating fluid type.

It can be seen from the Figure 4.3 that P-wave velocities slightly decrease in Garn Fm and Ile Fm. It goes from 3500 m/s to 3000 m/s at the interface between Melke Fm and Garn Fm.

4.4.5 Vp/Vs log

Vp/Vs log is the ratio between compressional velocity and shear velocity. The Vp/Vs ratio has been used for many objectives, such as lithology indicator, determining the degree of consolidation and identifying pore fluid. The fact that P-

wave velocity decreases and S-wave velocity increases with the increase of light hydrocarbon saturation makes the ratio of Vp/Vs more sensitive to the change of fluid type than the use of Vp or Vs separately.

Normally for most consolidated rock materials, Vp/Vs is below 2. The seismic Vp/Vs ratios for sandstones in the three wells varied between 1.66 to 1.81and for carbonates, 1.81 to 1.98.

Figure 4.6, 4.7, and 4.8 show Vp/Vs ratio log for well 6507/11-9, 6507/11-8, and 6507/11-1, respectively. We can observe that there is a slightly decrease in Vp/Vs value in Garn Fm for both of well 6507/11-9 and well 6507/11-8. Vp/Vs value also decreased in Ile formation at well 11-8. There is no significance drop value of Vp/Vs for well 6507/11-11. This low value of Vp/Vs (1.5 – 1.65) is typically interpreted as an indication of hydrocarbon bearing rocks, if it coincides with relatively low acoustic impedance values.

4.4.6 Acoustic Impedance log

Acoustic impedance is basically the product between P-wave velocity and bulk density. The main application of acoustic impedance log is lithology and pore fluid prediction.

We can observe from Figure 4.6 that acoustic impedance value is slightly decreasing in Garn Fm and Ile Fm for both of well 6507/11-8 and 6507/11-9. This possibly happens due to lithology and porosity effect, as increasing porosity can reduce acoustic impedance.

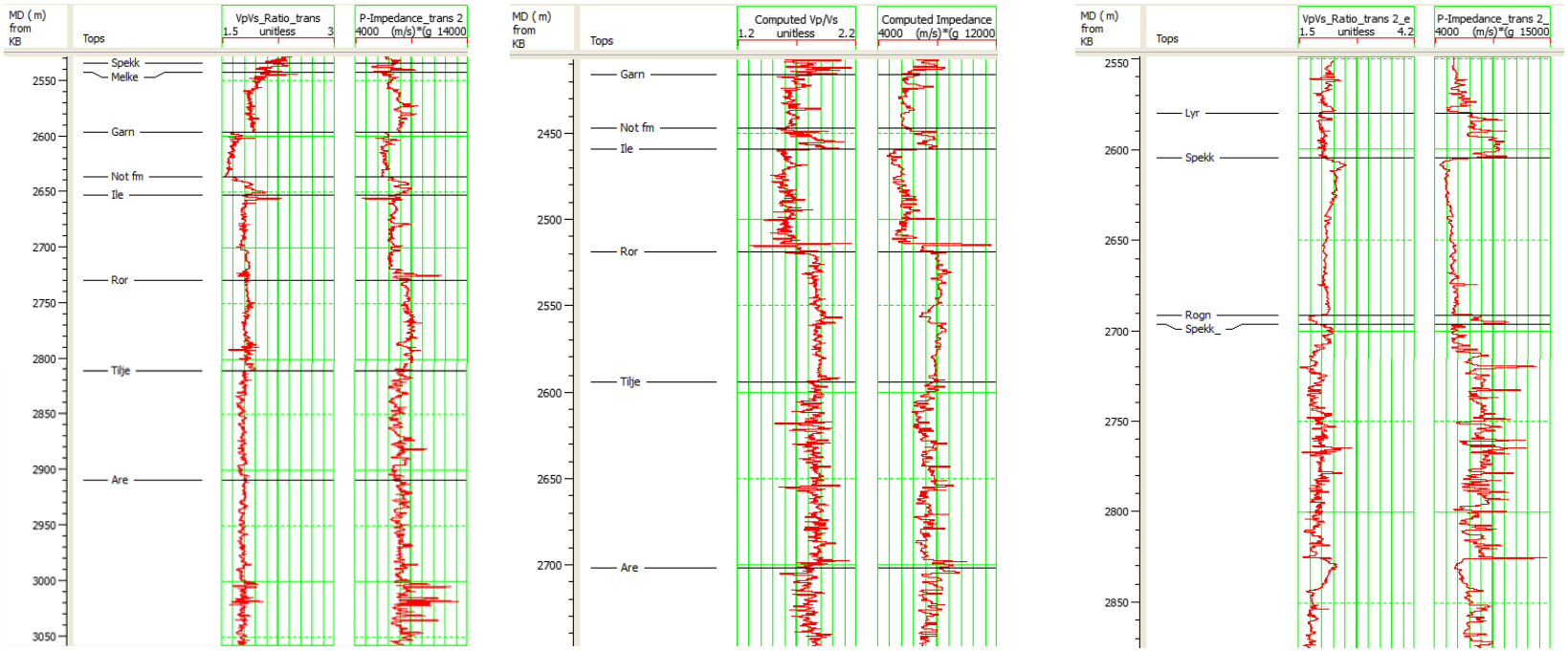

Figure 4.6: From left to right: VpVs and Acoustic Impedance logs for well 6507/11-9, 6507/11-8 and 6507/11-11, respectively.

4.5 RPT analysis of well log data

The main motivation behind RPT(s) is to use theoretical rock physics trends for the different lithologies expected in the area instead of using additional log data to aid interpretation. The ideal interpretation workflow for RPT analysis is divided into two-step simple procedure. First, use well log data to verify the validity of the selected RPT(s). Then use selected and verified RPT(s) to interpret elastic inversion results (Avseth et al., 2005).

The most common form of RPT is the cross-plot between Vp/Vs and acoustic impedance (AI). This will allow us to perform rock physics analysis not only on well-log data but also seismic data such as elastic inversion results. RPT interpretation of well-log data may also be an important stand-alone exercise, for interpretation and quality control of well-log data, and in order to assess seismic detectability of different fluid and lithology scenarios (Avseth et al., 2005).

RPT(s) model have to honor local geological factors. Geological constraints on rock physics models include lithology, mineralogy, burial depth, diagenesis, pressure and temperature. The parameters that are used for the RP model can be seen from table 4.3.

Table 4.3: The parameters used in RPT model.

Summary of the parameters that used in RPT model	
Critical porosity = 0.4	Kdry = 1.97 Gpa
Coordination number = 8.64	μdry = 2.9 Gpa
Effective pressure = 0.022 GPa	Density = 2.64 g/cc

Figure 4.7 shows the corresponding Vp/Vs vs AI cross-plot from well 6507/11-9 superimposed onto appropriate RPT. The upper shale-trend line represents pure shale while the below sand-trend line represents clean compacted brine filled quartz sand. There is also a line representing increasing gas saturations which is almost perpendicular to the sand-trend line. The logs are color-coded based on the five populations defined in the cross-plot domain.

Separate lithology can be attributed to each five populations based on additional log information: two different shales, gas sand, brine sand, and limestone. These two shale populations represent shales with different stiffness. The softest shale is Spekk Fm and the stiffest shale is Melke Fm, Not Fm, and Ror Fm. Spekk Fm organic rich shales consistently plotting above the brine sand population in every well. Assuming that the selected RPT(s) is valid for this area, the gas sand appears to have about 28-30% porosity and the brine sand 25-33% porosity.

The cross-plot also shows a very good separation between gas sand of Garn Fm and brine sand of Ile Fm and Ror Fm. The brine sand population plots just above the theoretical brine sand trend. The gas sand population plots well in the hydrocarbon area below brine sand trend and around the dotted lines indicating the effects of increasing gas saturation. This complies with what we define in the RPT template that the hydrocarbon plots nicely in the area of the template where we expect hydrocarbon rocks to plot at this burial depth.

Figure 4.8 shows Vp/Vs vs AI cross-plot from well 6507/11-8 which is located southeast from well 6507/11-9. The fluid sensitivity of Vp/Vs and AI is also significant, and we detect a large drop in both Vp/Vs and AI from the gas sand population (Garn Fm and Ile Fm) relative to shales population (Not Fm and Ror Fm). At this well location, the AI and Vp/Vs estimation is not measured up until the Spekk Fm. However, the other well in this area that penetrates Spekk Fm have the value of S-wave velocity.

The Ile Fm at well 11-8 plots below the brine sand trend with relatively low Vp/Vs value. It is different from the well 6507/11-9 which plots just above brine sand trend. This happens because Ile Fm is brine saturated in well 6507/11-9 and gas saturated in well 6507/11-8.

Figure 4.9 shows the Vp/Vs vs AI cross-plot together with well log data from well 11-11. A thick 100 m Spekk Fm was encountered below a hard carbonate layer of Lyr Fm. This organic rich shale was found to be immature and had relatively high Vp/Vs value. There is no gas sand population appearing in this well. However, there is a thin Rogn Fm encountered near the base of the Spekk Fm which plots just above the brine sand trend with relatively low Vp/Vs value.

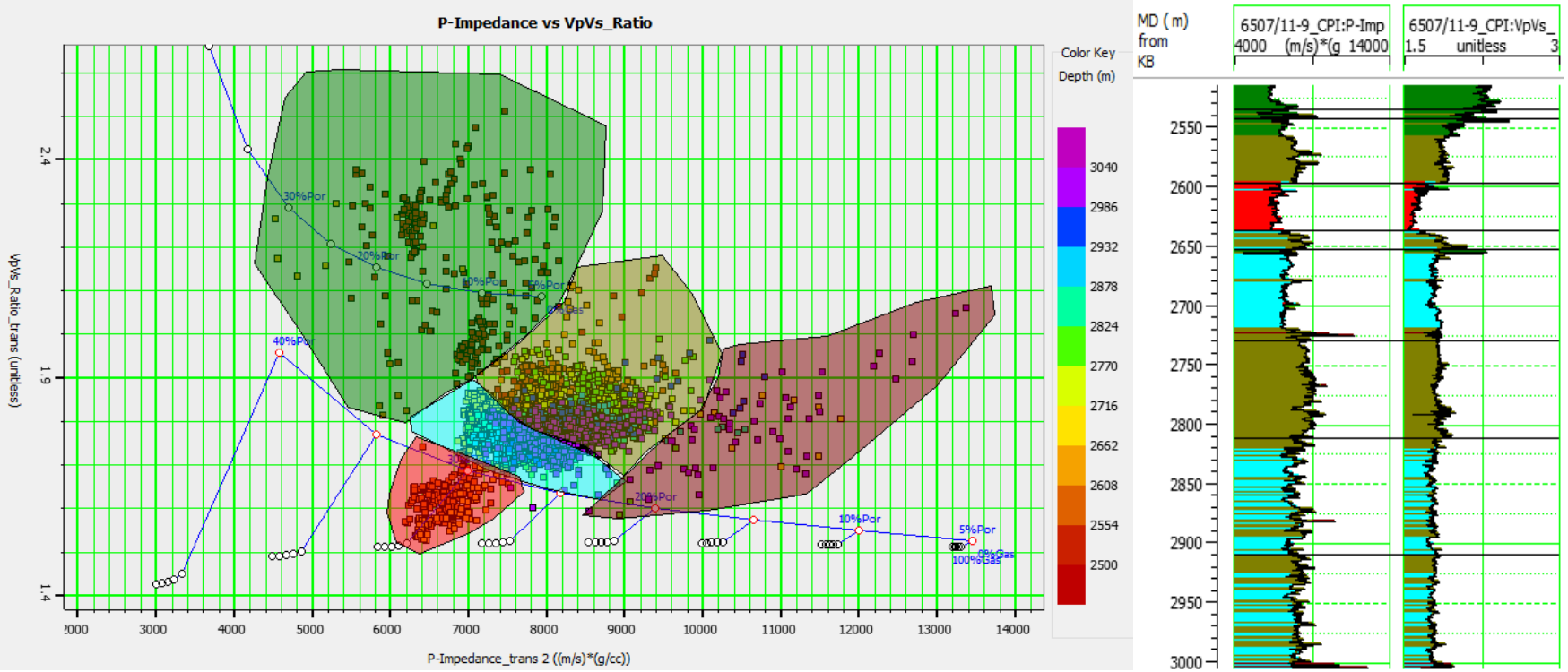

Figure 4.7: AI and Vp/Vs logs (right) and Vp/Vs vs AI cross-plot (left) for well 6507/11-9. The logs are color-coded based on the populations defined in the cross-plot domain.

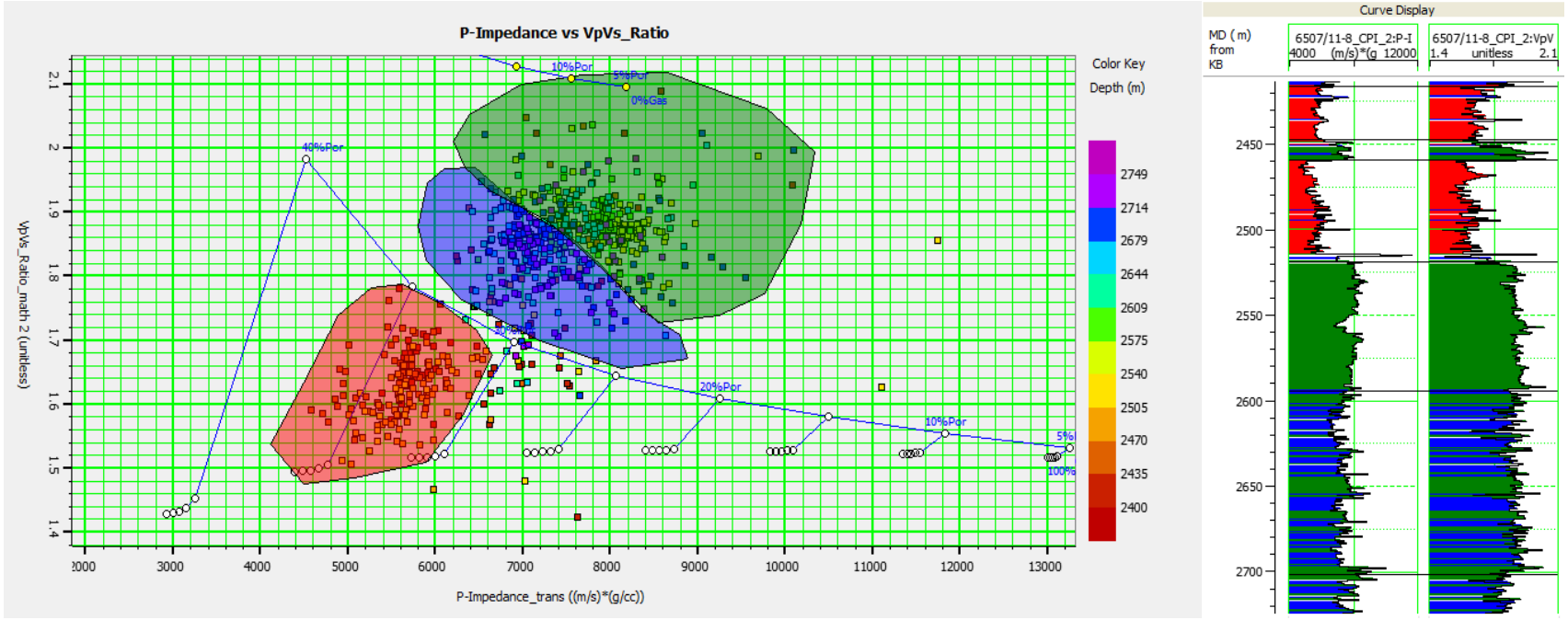

Figure 4.8: AI and Vp/Vs logs (right) and Vp/Vs vs AI cross-plot (left) for well 6507/11-8.

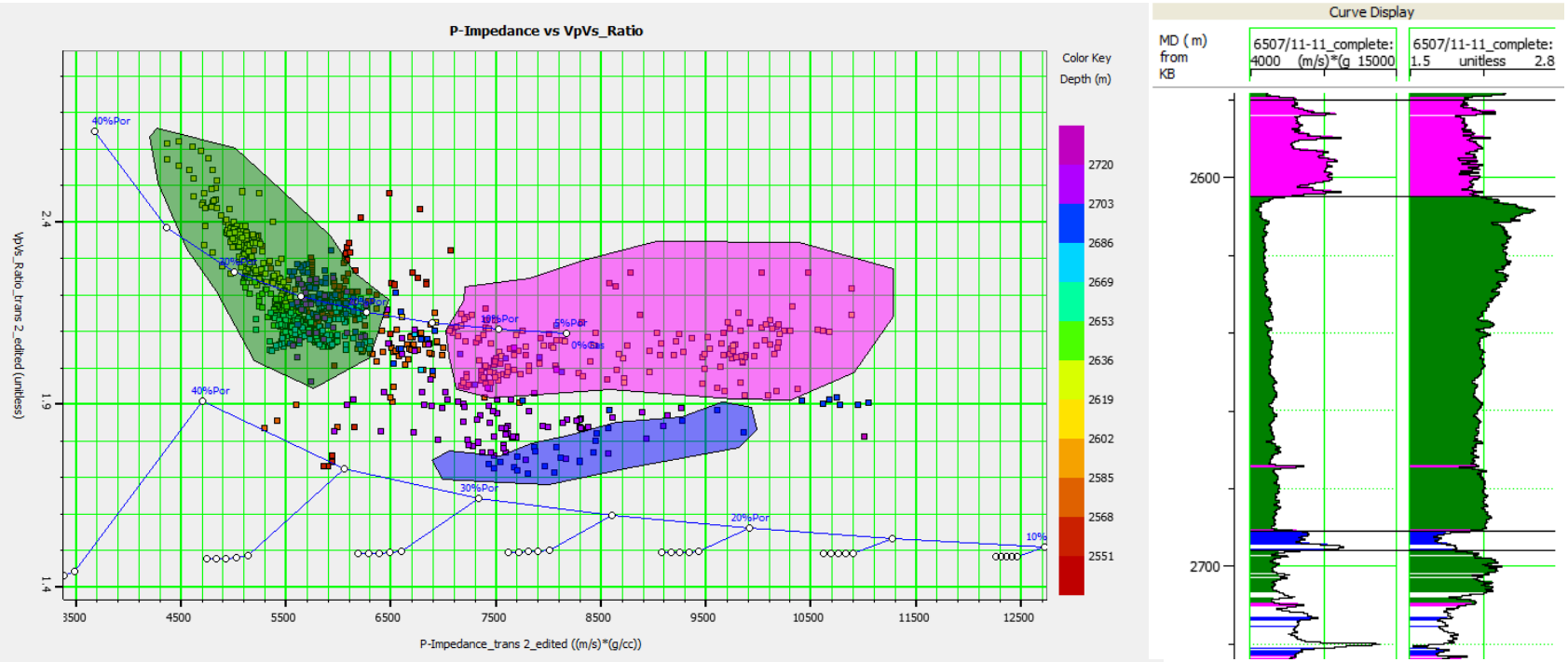

Figure 4.8: AI and Vp/Vs logs (right) and Vp/Vs vs AI cross-plot (left) for well 6507/11-11.

4.6 Interpretation of elastic inversion

Simultaneous AVO inversion data calibrated to the Zumba well (6507/11-11) is available for this study (see also Avseth et al., 2016). Partial stacks have been inverted directly for AI and Vp/Vs using a 3-term Aki-Richard approximation to the Zoeppritz equations. The gas and oil discoveries in this study area have good class II to III AVO signatures. Figure 4.10 shows the Vp/Vs and AI at the well 6507/11-8 location. We can observe that the inserted upscaled well log data are matching with the elastic inversion results. The hydrocarbon bearing rocks are interpreted as low AI and Vp/Vs value so we can analyze the reservoir distribution by qualitative interpretation.

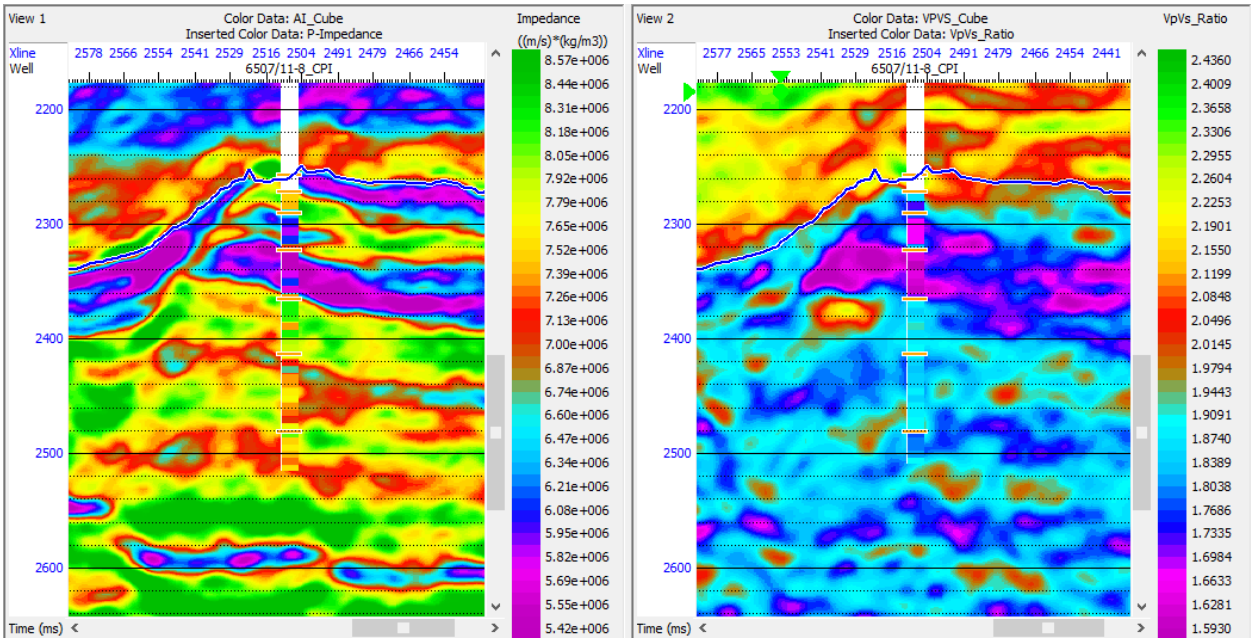

Figure 4.10: Seismic inversion result at the well 6507/11-8 location, including acoustic impedance (left) and Vp/Vs (right).

4.7 Classification inversion using RPT templates

Figure 4.11 shows the Vp/Vs vs AI cross plot of the elastic inversion results with the selected RPT(s) template superimposed. The cross-plot only contains the data within 200 ms below the BCU interpreted horizon, since the zone interest in this study is beneath BCU surface. We can observed that we don't see the same scattering population as for the log cross-plotting, which should be the effect of lower depth resolution in the seismic data. But still the interpretation of cross-plot population appears to be quite similar. The population that plots along theoretical shale trend is interpreted as shale and brine sand trend is interpreted as brine sand. The points between the shale and brine-sand trends are interpreted to be shaly sand.

Ten populations interpreted as separate lithology based on well log data information:

- stiff shale (olive polygon) : high Vp/Vs and intermediate AI values
- soft shale (green polygon): high Vp/Vs and low AI values
- marl (gray polygon) : intermediate to high Vp/Vs and intermediate AI values
- hot shale (light green) : intermediate to high Vp/Vs and low AI values
- stiff brine sand (cyan polygon) : low to intermediate Vp/Vs and intermediate AI values
- soft brine sand (blue polygon) : low to intermediate Vp/Vs and low AI values
- shaly sand (dark cyan polygon) : intermediate Vp/Vs and intermediate AI values
- stiff gas sand (orange polygon) : low Vp/Vs and intermediate AI values
- soft gas sand (red polygon) : low Vp/Vs and low AI values
- limestone (magenta polygon) : intermediate Vp/Vs and very high AI values

The polygons are somewhat different from the polygons in well log data domain. This is because the seismic data contain a larger variability in facies compare to well log data and we want to an emphasis on the texture-related changes. This advantage made it easier to interpret facies which are not included in the wells.

The variation of sandstone in this study area is associated with depositional burial trends. For example, we separated the gas sand into two sand facies with different porosity or compaction. We are grouping it into different sand facies in order to honor geological trends in the elastic inversion results.

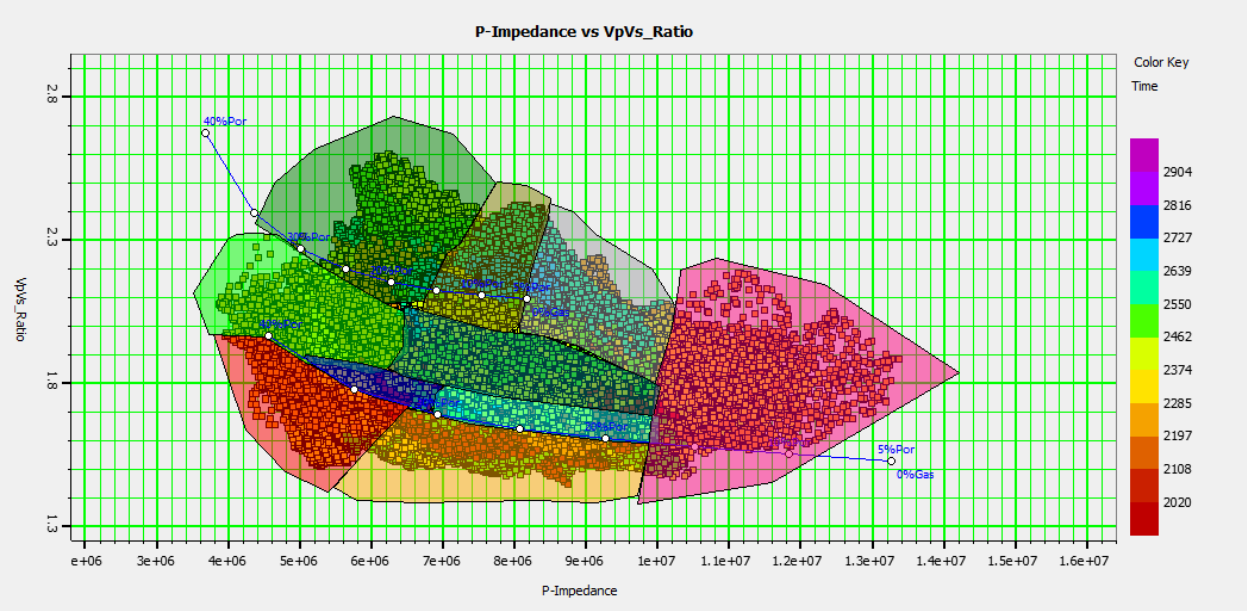

Figure 4.9: Cross-plot of acoustic Impedance versus Vp/Vs derived from seismic data superimposed onto the same RPT that was validated with well log data.

Figure 4.12and Figure 4.13 shows the section of RPT classified lithofacies compared to elastic inversion results at the well 6507/11-8 and well 6507/11-11 location, respectively. We can observe that the soft gas sand population (red polygon) matches very well with the low AI and low Vp/Vs values at well 6507/11-8 which is interpreted as gas sand from Garn Fm and Ile Fm. The thick organic rich shale (Spekk Fm) also matches quite well with the hot shale population from RPT classified lithofacies at the well 6507/11-11 location. Also, note that the very hard, carbonaceous Lyr Fm right above Spekk Fm is clearly visible as the gray colored layer.

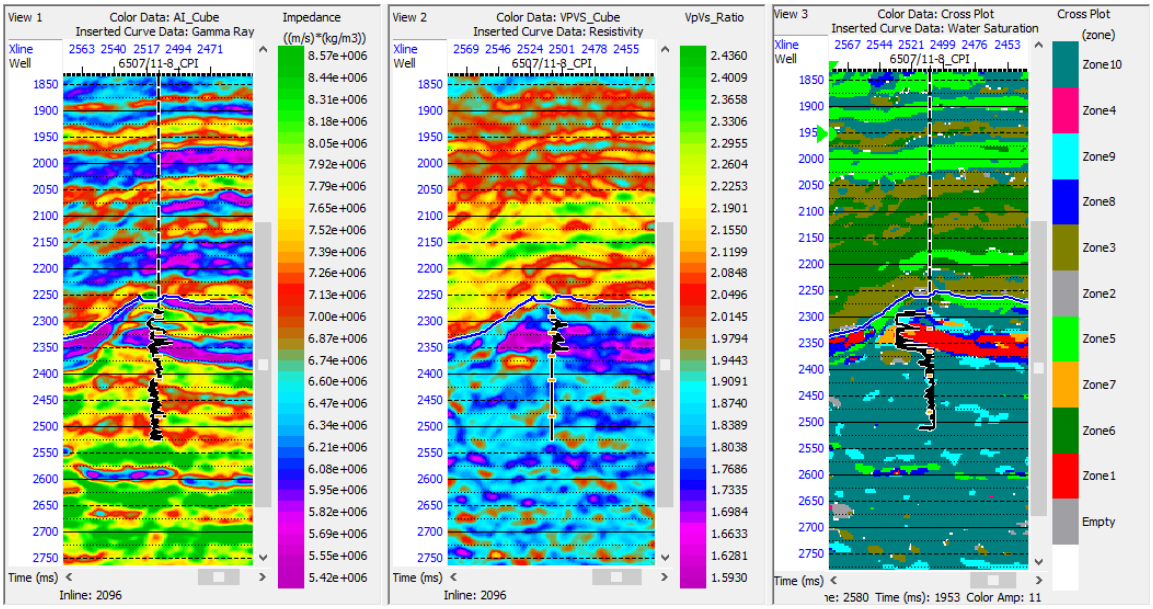

Figure 4.12: From left to right: AI inversion superimposed with GR log, Vp/Vs inversion superimposed with resistivity log, RPT classified lithofacies superimposed with saturation log at well 6507/11-8 location

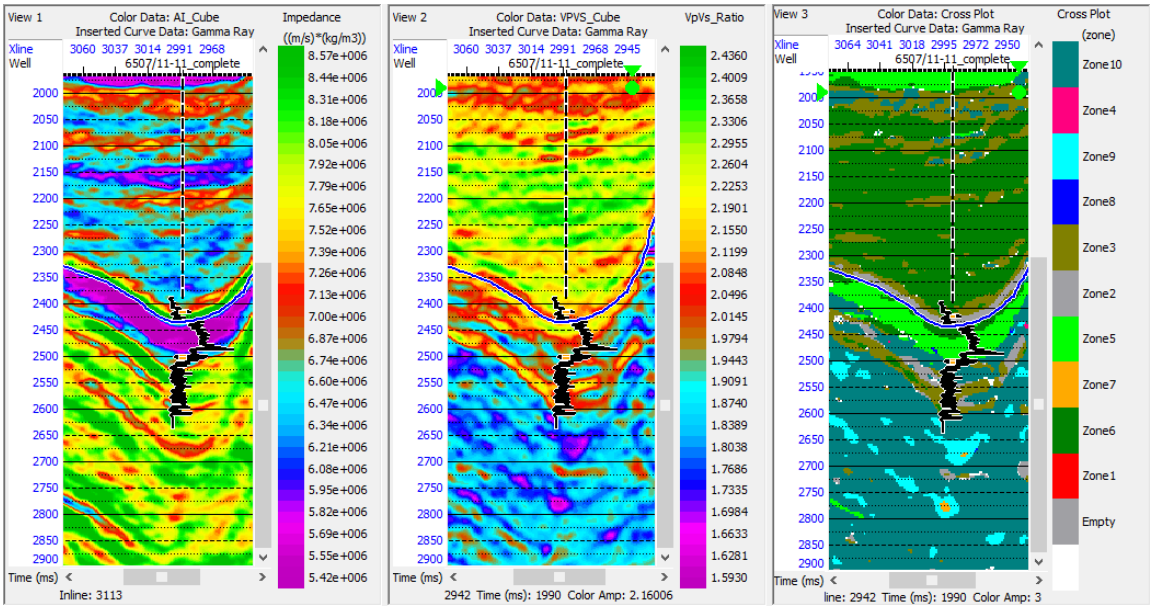

Figure 4.13: From left to right : AI inversion superimposed with GR log, Vp/Vs inversion superimposed with GRlog, RPT classified lithofacies superimposed with GR log at well 6507/11-11 location.

4.8 Estimated Rock physics attribute

Avseth et al. (2014) introduce CPEI and PEIL attributes that complied with calibrated rock-physics models. CPEI is sensitive to fluid-relation, whereas PEIL is related to rock stiffness. Using the rock-physics attributes defined earlier, we obtain the corresponding CPEI and PEIL attributes as shown in Figure 4.14.

The PEIL attribute correlates with rock stiffness and not dependent on pore fluid content. Some soft anomalies can be seen right below the horizon, which represents the Base Cretaceous Unconformity. This event can also be seen on the acoustic impedance section. These are likely organic rich-shales of Spekk Fm. However, these cannot be seen clearly on the CPEI attribute.

In the CPEI attribute, we can observe the gas discovery encountered by the 6507/11-8 well intersected by the seismic section. It brightens up and shows a nice correlation with the saturation log of well 6507/11-8.

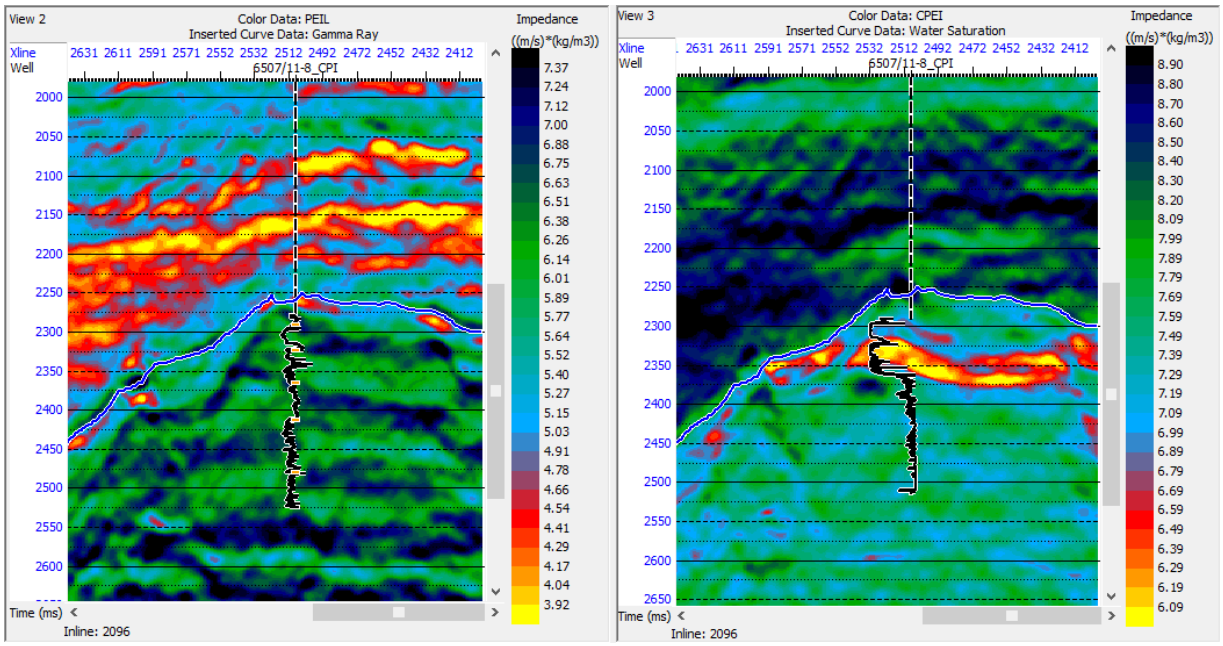

Figure 4.10: The PEIL (left) superimposed with GR log and CPEI (right) superimposed with saturation log at well 6507/11-8 location.

5. Results

Ten facies were interpreted from RPT analysis in the study area: stiff shale, soft shale, hot shale, marl, stiff brine sand, soft brine sand, stiff gas sand, soft gas sand, shaly sand, and limestone. This variation based on an assumption of various lithofacies or rock types.

Cross sections intersecting both Yttergryta and Natalia structures with classification result based on the RPT analysis and the CPEI attribute are shown in Figure 5.1 and Figure 5.2, respectively. The reservoir sand in Yttergryta structure from Garn Fm and Ile Fm are identified in both sections which are showed as low CPEI value and a gas sand facies.

There seems to be indications of hydrocarbon-filled sandstones in the graben area and near the Natalia structure. Both of these sandstones are most likely from Garn Fm. Another interesting anomaly is in the terrace area just west of the structural high. This anomaly is within the Upper Jurassic age. This sand accumulation is interpreted as submarine lobes and fans that were eroded sands from a high structure which were deposited around the flanks.

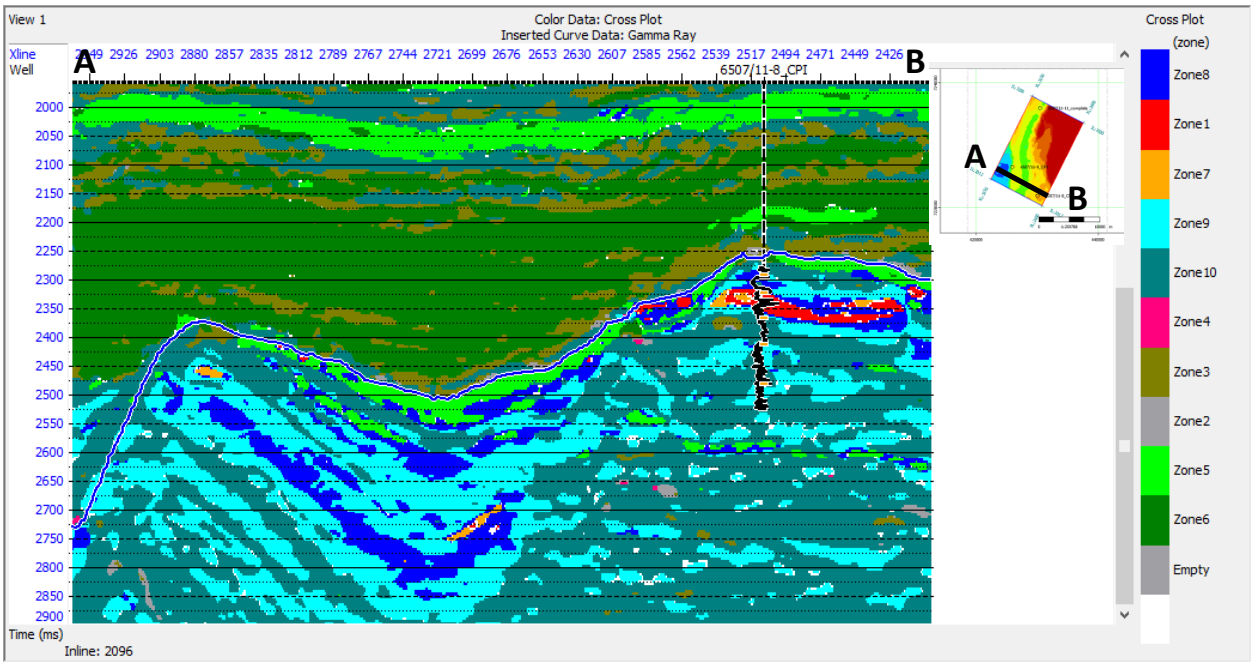

Figure 5.1: RPT classified lithofacies section intersecting with well 6507/11-8.

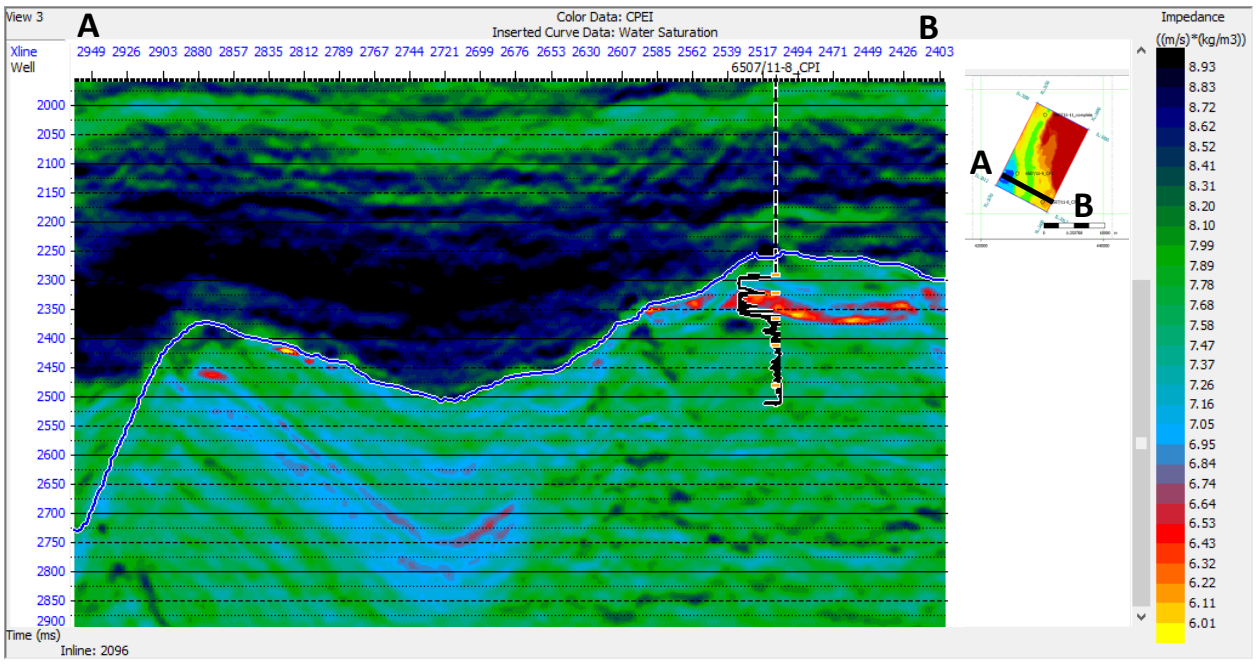

Figure 5.2: CPEI section intersecting with well 6507/11-8.

The thin Rogn Fm in the well 6507/11-11 is observed to be progressively thicker further south (Fig.5.3). There is a possibility of by-passed Rogn Fm sand that has been deposited further south. The Rogn Fm could have been deposited as a turbidite system along the graben. The turbidite flows were able to transport the eroded sediment towards the south. However, it is less likely to be filled with hydrocarbon since there is no strong indication of hydrocarbon presence both from RPT classified lithofacies and CPEI attribute sections in the graben area. However, this intra-Spekk Fm shows a good indication of hydrocarbon anomaly in the terrace area suggesting a hydrocarbon preferential migration pathway.

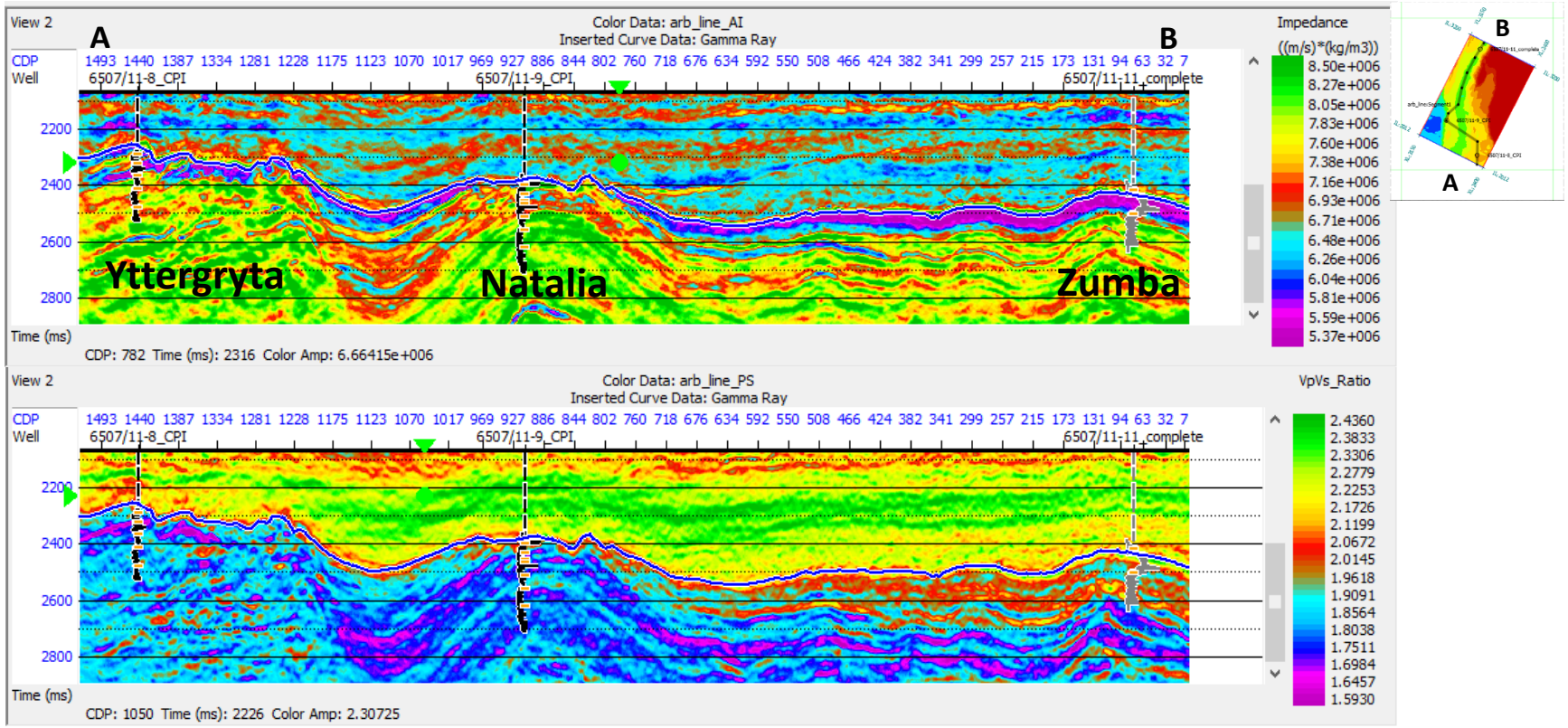
View 2
A
Color Data: arb_line_AI
Inserted Curve Data: Gamma Ray
B
CDP
Well
1493 1440 1387 1334 1281 1228 1175 1123 1070 1017 969 927 886 844 802 760 718 676 634 592 550 508 466 424 382 341 299 257 215 173 131 94 63 32 7
6507/11-8_CPI
6507/11-9_CPI
6507/11-11_complete
2200
2400
2600
2800
Yttergryta
Natalia
Zumba
Time (ms)
CDP: 782 Time (ms): 2316 Color Amp: 6.66415e+006
Impedance
((m/s)*(kg/m3))
8.50e+006
8.27e+006
8.05e+006
7.83e+006
7.60e+006
7.38e+006
7.16e+006
6.93e+006
6.71e+006
6.48e+006
6.26e+006
6.04e+006
5.81e+006
5.59e+006
5.37e+006
View 2
Color Data: arb_line_PS
Inserted Curve Data: Gamma Ray
VpVs_Ratio
CDP
Well
1493 1440 1387 1334 1281 1228 1175 1123 1070 1017 969 927 886 844 802 760 718 676 634 592 550 508 466 424 382 341 299 257 215 173 131 94 63 32 7
6507/11-8_CPI
6507/11-9_CPI
6507/11-11_complete
2200
2400
2600
2800
Time (ms)
CDP: 1050 Time (ms): 2226 Color Amp: 2.30725
2.4360
2.3833
2.3306
2.2779
2.2253
2.1726
2.1199
2.0672
2.0145
1.9618
1.9091
1.8564
1.8038
1.7511
1.6984
1.6457
1.5930
B
A

(a)

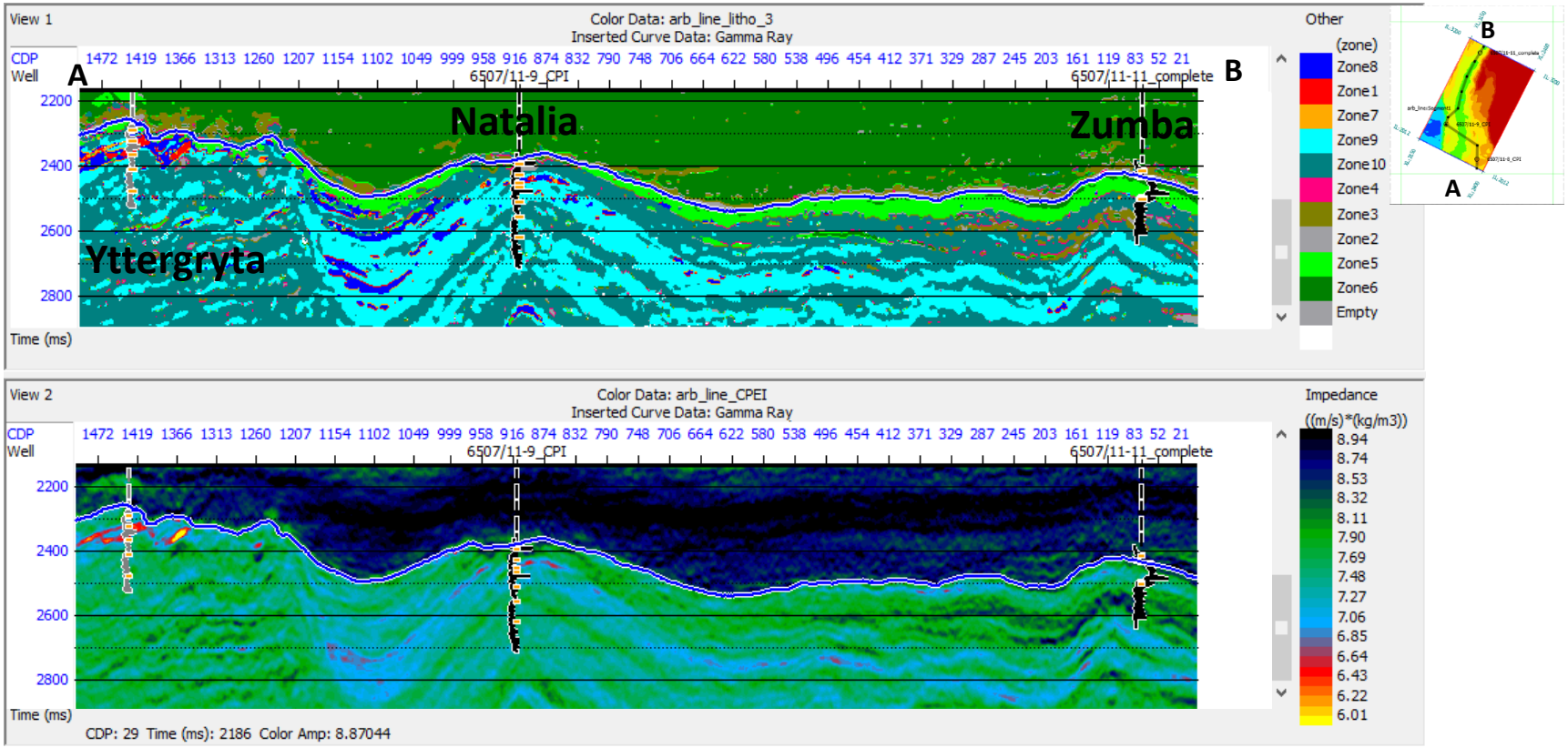

(b)

Figure 5.11: Random seismic section intersecting all 3 wells in this study showing (from top to bottom): (a) AI inversion and Vp/Vs inversion results (b) RPT classified lithofacies and CPEI attribute.

A data slice was created based on 100 ms below the BCU horizon for both RPT classified lithofacies and CPEI attribute. Figure 5.4 shows the horizon slice map view of RPT classified lithofacies which showing the lateral distribution of various lithology facies. The gas sand population is well distributed in the Yttergryta structure and the Natalia structure. The indication of hydrocarbon filled sandstone is can be seen on the horizon slice map view of CPEI attribute (Fig. 5.5).

Furthermore, gas sand population is detected in the southern part of Zumba graben but no apparent strong anomaly from CPEI attribute. This population extends along the whole graben area and pinches out towards the north.

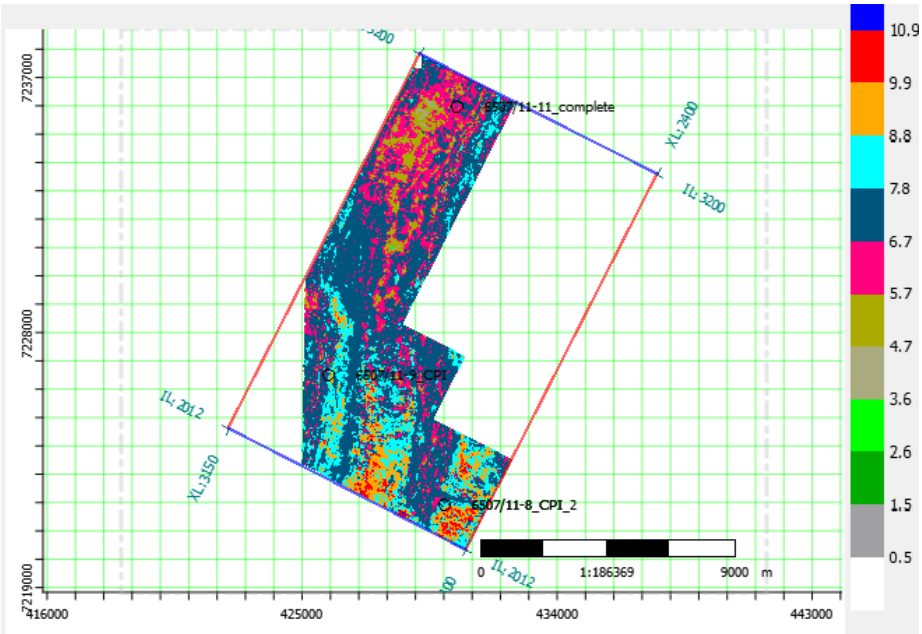

Figure 5.4: Horizon slice map from RPT classified lithofacies.

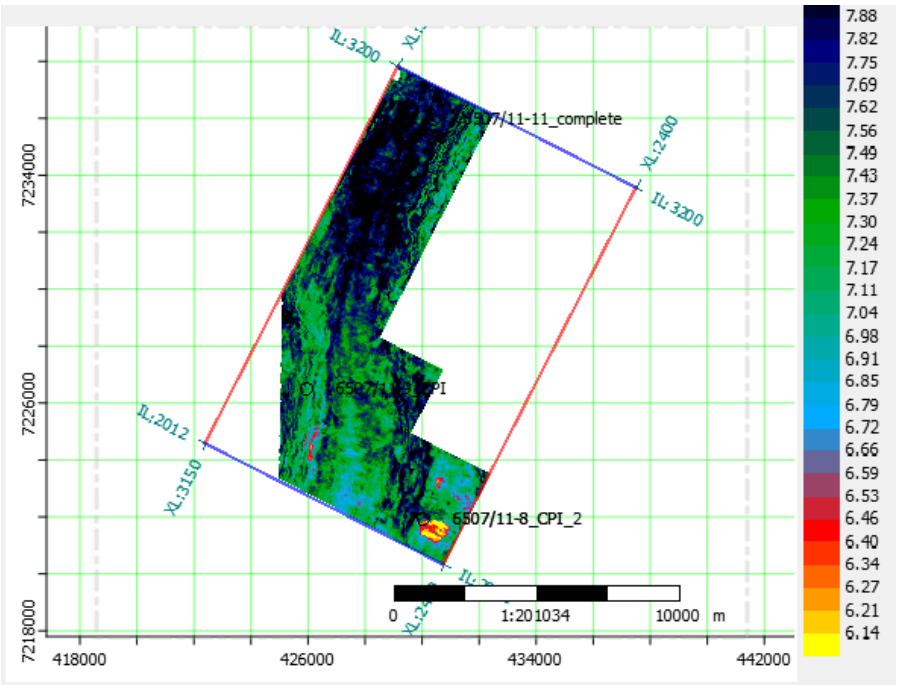

Figure 5.5: Horizon slice map from CPEI attribute.

6. Discussion

This study is mainly focused on Rock Physics Template (RPTs) as a toolbox for interpretation of well log data and elastic inversion results. There are some uncertainties during the analysis that are related to well-log data, elastic inversion results, and rock physic.

The well-log data uncertainties are associated with the acquisition and processing. Many errors may occur in well log measurement even though there is a correction for each log. Porosity, water saturation, and shale content are logs that are typically not directly measured by well logging tools. They are derived through multiple processes. As each of these steps involves uncertainty, the resultant petrophysical data will have uncertainty and limitations.

The example of data acquisition uncertainties is shown in Figure 6.1. Caliper log curve shows a bad borehole quality which brings some uncertainty to measured log curve sonic log.

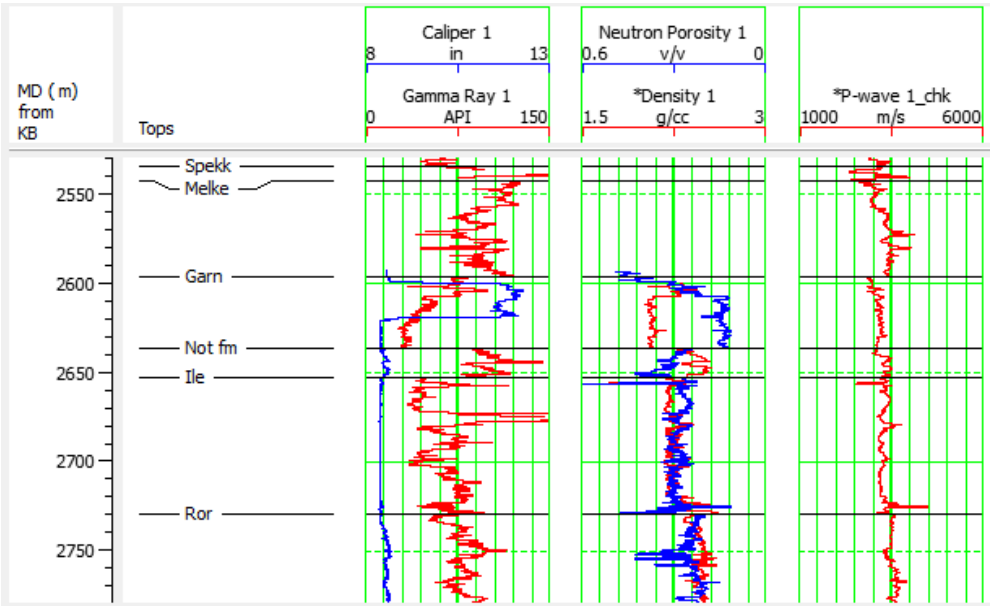

Figure 6.1: From left to right: Caliper log superimposed with GR log, density-neutron, P-wave velocity.

The elastic inversion results are non-unique. It means that there are a large number of possible solutions would give the same seismic response. Furthermore, the limitation to the inversion is the assumption of isotropic media and the weak-contrast approximation to Zoeppritz equation. The low frequency model is also the key feature for building the model during the simultaneous AVO inversion. It is generated from well log data and seismic interval velocities. Away from well control, the low frequency model is more unreliable. The greater number of wells to create the low frequency model will make the model better. The elastic inversion results for this study have been updated with the new well 6507/11-11 which was drilled last year.

The most common uncertainties for rock physics model are model assumptions and input parameters. Hertz-mindlin has an assumption of perfect sediment grains, identical spheres, which is never found in a real sample. Furthermore, the presence of low gas saturation could give same AVO signature with commercial gas saturation.

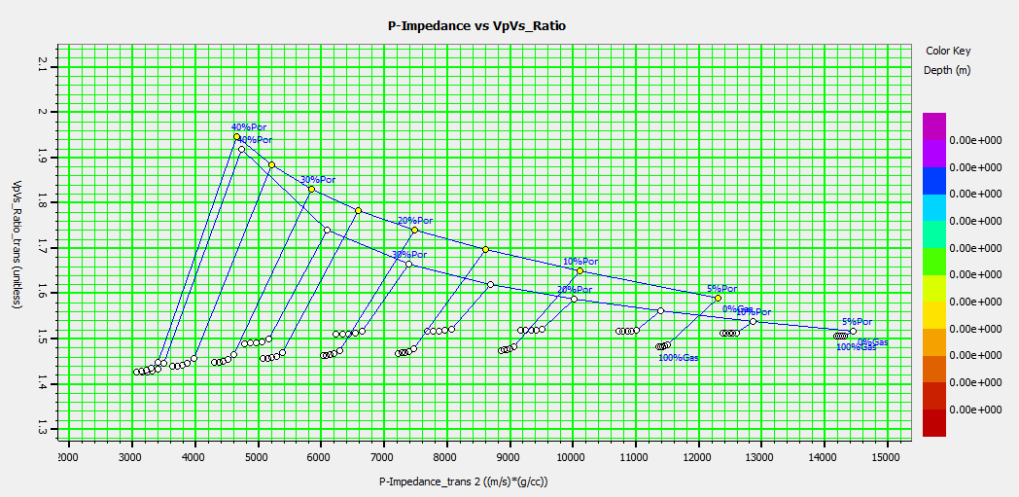

Figure 6.2: Cemented superimposed with unconsolidated RPT template.

7. Conclusion

This study has demonstrated how Rock physics template (RPTs) analysis can be a useful tool for lithology and pore fluid interpretation of well log data and seismic inversion results. The analysis divided into two steps. Firstly, use the well log data to verify the validity of the selected RPT(s). Secondly, use selected and verified RPT(s) to interpret elastic inversion results.

We can also use rock physics template (RPT) to create rock physics attributes (CPEI and PEIL) that can be utilized to screen seismic inversion for rock quality and hydrocarbon saturation.

The results show that we can potentially distinguish between different types of lithology facies in the study area. We are also able to delineate and predict potential hydrocarbon accumulations and possible remaining prospectivity in the Grinda Graben in the Norwegian Sea.

A high potential prospect was defined along the high structure of both Natalia and Yttergryta in Garn Fm level. There is a possibility of hydrocarbon-filled sandstones in the terrace area just west of the Yttergryta high structure. This sand accumulation is interpreted as submarine lobes and fans that were eroded sands from a high structure which were deposited around the flanks. Further south of the well 6507/11-11, a gas sand population can be detected along the axis of the graben area.

References

Aki, K.T., and Richards, P.G., 1980, Quantitative Seismology: Theory and Methods: Vol. 1, W.H. Freeman and Co.

Avseth, P., and Veggeland, T., 2015, Seismic screening of rock stiffness and fluid softening using rock-physics attributes, Interpretation, 3(4), SAE85-SAE93.

Avseth. P., Veggeland, T., and Horn, F., 2014, Seismic screening for hydrocarbon prospects using rock-physics attributes, The Leading Edge, 33(3), 266–268, 270–272, 274.

Avseth, P., Mukerji, T., and Mavko, G., 2005, Quantitative seismic interpretation – Applying rockphysics tools to seismic interpretation risk: Cambridge University press.

Avseth. P., Janke,A., and Horn, F., 2016, AVO inversion in exploration – Key learnings from a Norwegian Sea prospect, The Leading Edge, 35(5), 405-414, 412-414, doi : 10.1190/tle35050405.1.

Batzle, M., and Wang, Z., 1992, Seismic properties of pore fluids. *Geophysics*, **57**, 1396 -1408.

Castagna, J.P., and Smith, S.W., 1994, Comparison of AVO indicators: A modelling study, *Geophysics,* 59(12), pp.1849-1855.

CGG, AVO cross-plot, Retrieve from http://www.cgg.com/en/What-We-Do/GeoSoftware/Platform-Environment/AVO-Attribute-Extraction.

Chopra, S., and Castagna, J.P., 2014, *AVO*, SEG Books.

Hashin, Z. and Shtrikman, S., 1963, A variational approach to the elastic behavior of multiphase minerals. Journal of the Mechanics and Physics of Solids, 11, pp. 127-140.

Faleide, J.I., Tsikalas, F., Breivik, A.J., Mjelde, R., Ritzmann, O., Engen, O., Wilson, J., and Eldholm, O., 2008, Structure and evolution of the continental margin off Norway and the Barents Sea, *Episodes*, *31*(1), pp.82-91.

Ma, X.Q., 2002, Simultaneous inversion of prestack seismic data for rock properties using simulated annealing, *Geophysics*, *67*(6), pp.1877-1885.

Mavko, G., Mukerji, T., and Dvorkin, J., 2009, The Rock Physics Handbook: Tools for Seismic Analysis of Porous Media (Seconded.), Cambridge University Press.

Mindlin, R., 1949, Compliance of elastic bodies in contact, Journal of Applied Mechanics, 16, pp. 259-268.

Mukerji, T., Jørstad, A., Mavko, G., 1998, Near and far offset impedances: Seismic attributes for identifying lithofacies and pore fluids. *Geophysics.Res.Lett*., **25**, 4557-4560.

Murphy, W.F.III, 1982, Effects of microstructure and pore fluids on the acoustic properties of granular sedimentary materials, Unpublished Ph.D. thesis, Stanford University.

Norwegian Petroleum Directorate-Bulletin No 8, Structural elements of the Norwegian continental shelf. Part II: The Norwegian Sea Region, 1995.

NPD Fact maps, Retrieve from *http://gis.npd.no/factmaps/html_20/.htm*.

NPD Fact pages, Yttergryta well 6507/11-8, Retrieve from *http://factpages.npd.no/ReportServer?/FactPages/PageView/wellbore_exploration.htm*.

NPD Fact pages, Natalia well 6507/11-9, Retrieve from *http://factpages.npd.no/ReportServer?/FactPages/PageView/wellbore_exploration.htm*.

Ross, C.P. and Kinman, D.L., 1995, Nonbright-spot AVO: Two examples, *Geophysics*, *60*(5), pp.1398-1408.

Rutherford, S.R., and Williams, R.H., 1989, Amplitude-versus-offset variations in gas sands: Geophysics, 54, 680-688.

Shuey, R. T., 1985, A simplification of the Zoeppritz equations: Geophysics, 5O, 609-614.

Smith, G.C., and Gidlow, P.M., 1987, Weighted stacking for rock property estimation and detection of GAS, *Geophysical Prospecting*, 35(9), pp. 993-1014.

Tsikalas, F., Faleide, J.I., and Kusznir, N.J., Along-strike variations in rifted margin crustal architecture and lithosphere thinning between northern Vøring and Lofoten margin segments off mid-Norwa, *Tectonophysics* 458.1 (2008): 68-81.

Ostrander, W.J., 1984, Plane-wave reflection coefficients for gas sands at nonormal angle of incidence. *Geophysics*, 49(10), 1637-1649.

Rasmussen, K.B., Bruun, A.N., and Pedersen, J.M., 2004, Simultaneous seismic inversion, In *66th EAGE Conference & Exhibition*.

Reuss, A., 1929, Berechnung der Fliessgrenzen von Mischkristallen. Z, Angew. Math. Mech, v. 9, p. 49-58.

Ødegaard, E., and Avseth,P., 2004, Well log and seismic data analysis using rock physics templates: First Break, 22, 37-43, doi : 10.3997/1365-2397.2004017.

Voigt, W., 1910, Lehrbuch der Kristallphysik. Leipzig : Teubner.

Whitcombe, D. N., Connoly, P.A., Reagan, R.L., and Redshaw, T.C., 2002, Extended elastic impedance for fluid and lithology prediction. *Geophysics*, **67**, 52-66.

Wisconsin, 2014, Voigt and Reuss model, Retrieved from http://silver.neep.wisc.edu/~lakes/MSE541Fr.html.

Appendix

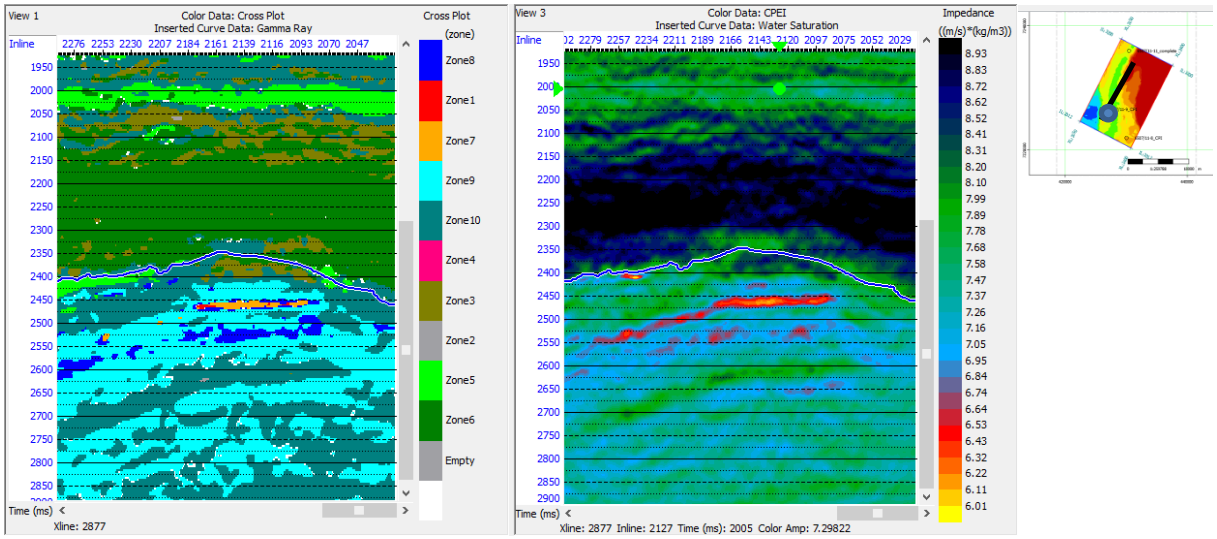

Figure A 1: Crossline section of RPT classified lithofacies (left) and CPEI attribute(right).

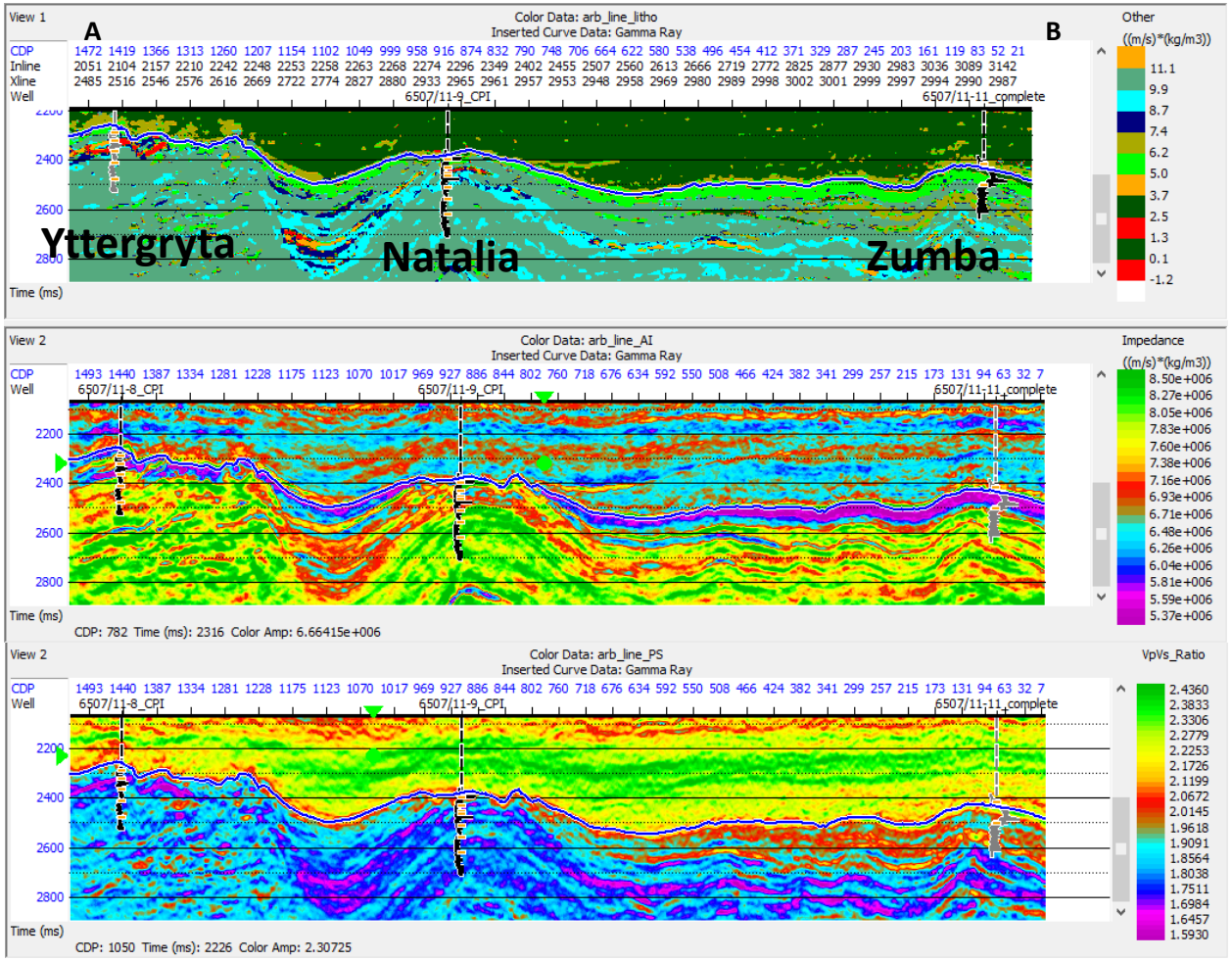

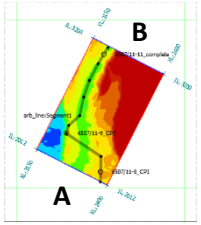

Figure A 2: Random seismic section intersecting all 3 wells in this study showing (from top to bottom): RPT classified lithofacies, AI inversion and Vp/Vs inversion results.

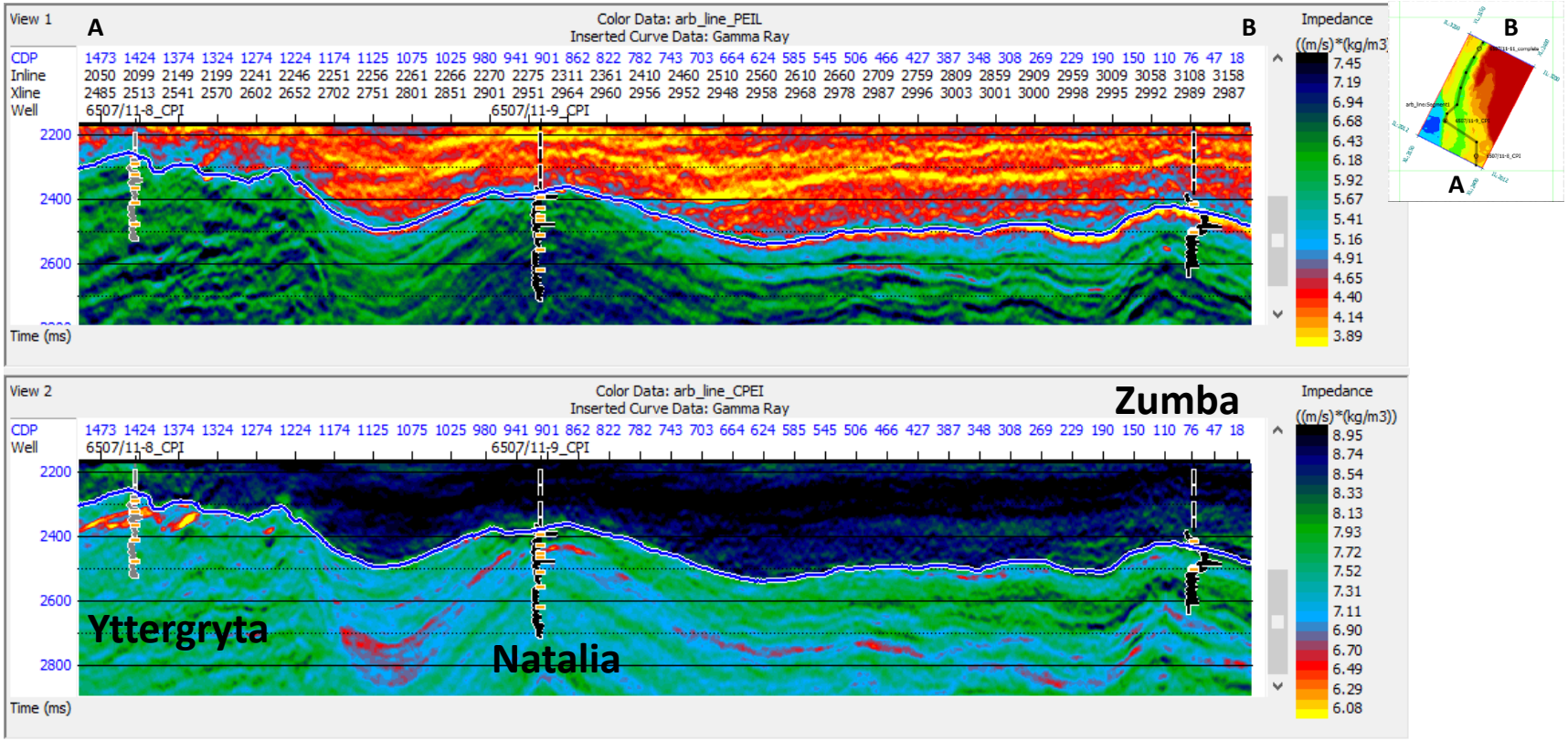

Figure A 3: Random seismic section intersecting all 3 wells in this study showing (from top to bottom): PEIL attribute, CPEI attribute.

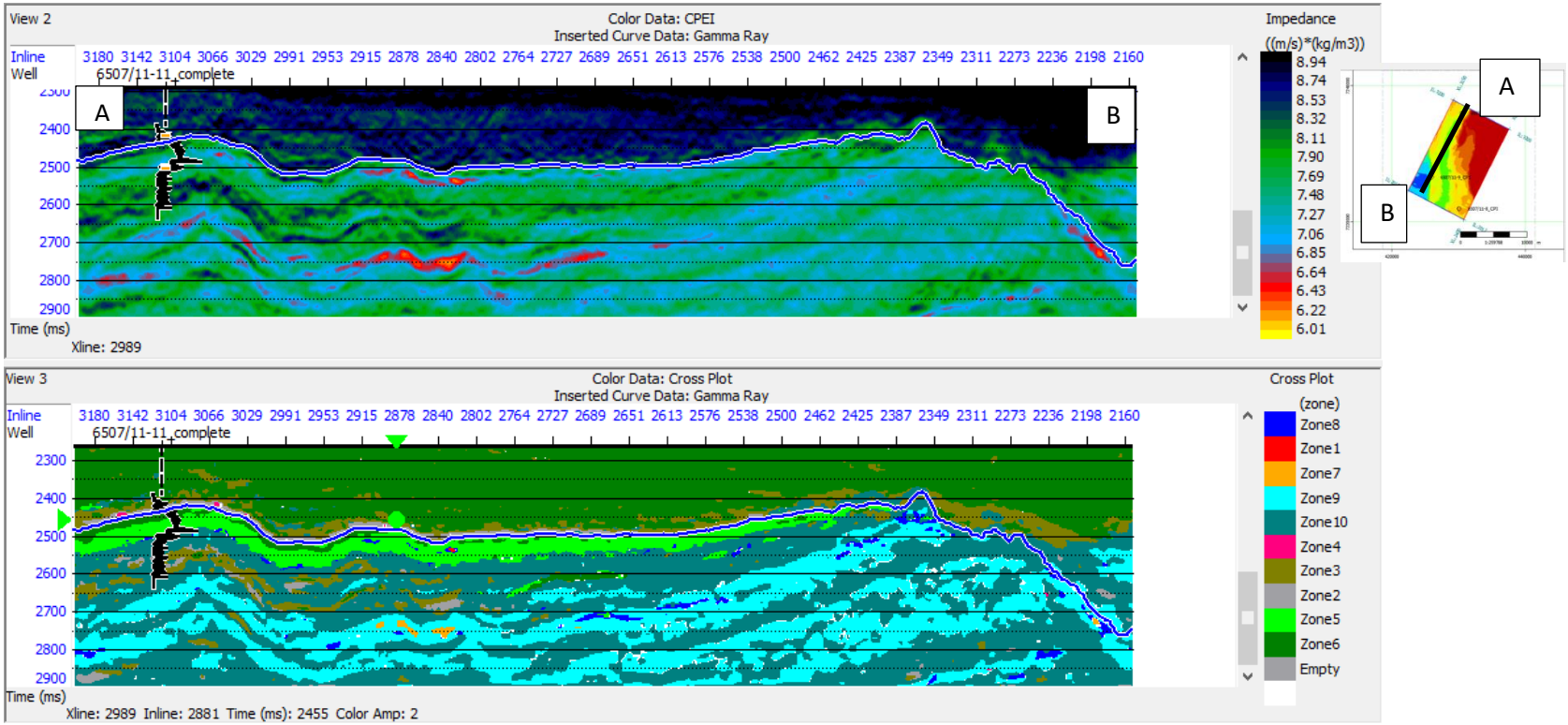

Figure A 4: Crossline section of CPEI (top) and PEIL (bottom) intersecting with well 6507/11-11.